# On the Decoherence of Two-Dimensional Spin Structures Coupled to an Electron Bath

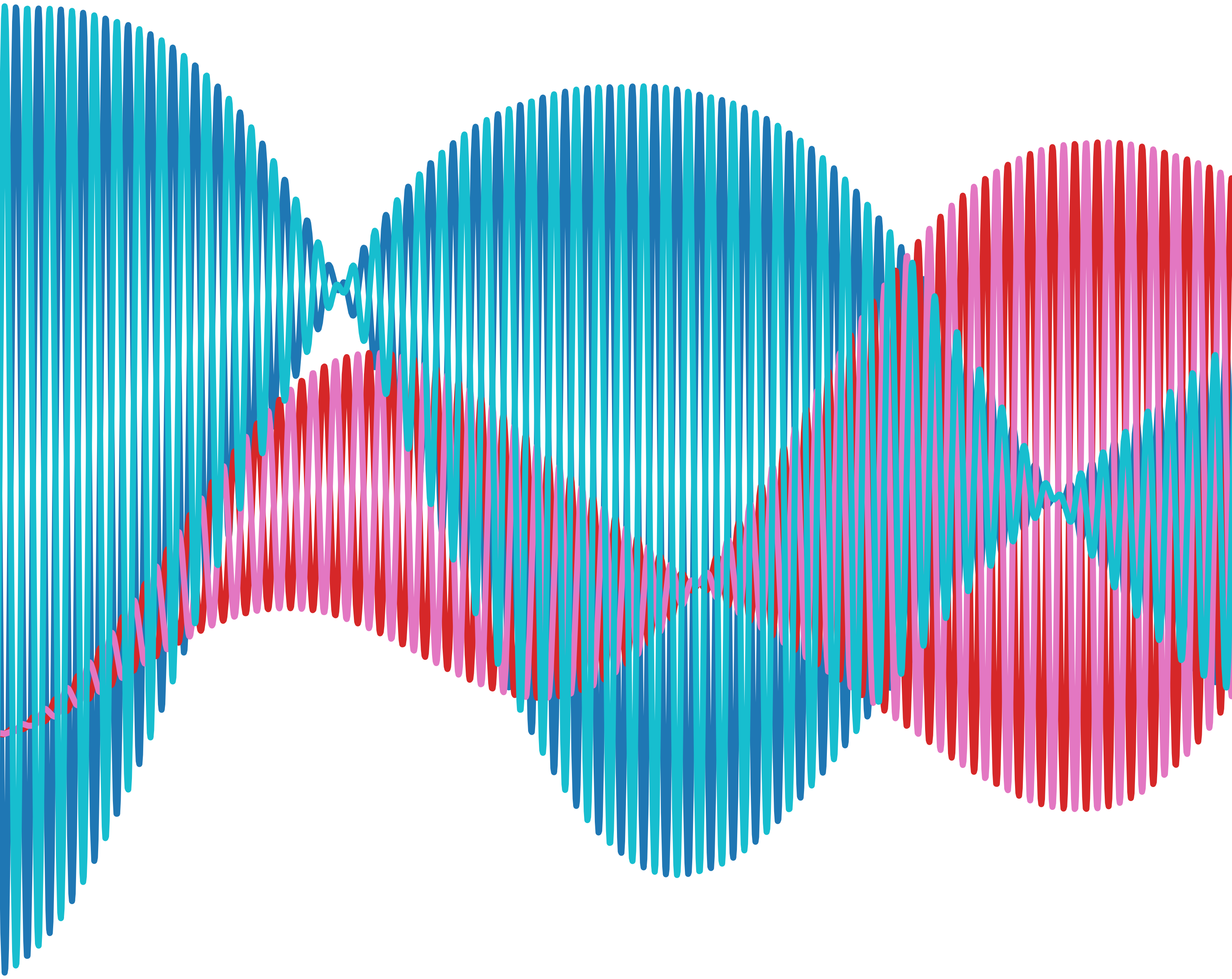

# DELFT UNIVERSITY OF TECHNOLOGY

BACHELOR THESIS
APPLIED PHYSICS & APPLIED MATHEMATICS

*to obtain the degree of Bachelor of Science*
*at Delft University of Technology,*
*to be defended publicly on Wednesday March 26, 2025 at 13:00 PM.*

*By:*
Tessa van Duin

*Supervisors:*
Paul Visser
Sander Otte

*Thesis Committee:*
Miriam Blaauboer
Wolter Groenevelt

Supporting documents to be found on:
`https://github.com/tessavanduin/Decoherence_2Dstructures.git`

April 3, 2025

## Abstract

Decoherence plays an important role in the evolution of quantum systems. In this thesis, we theoretically investigate the decoherence dynamics of two-dimensional spin-$\frac{1}{2}$ structures coupled to an electron bath, with a focus on the influence of exchange and dipolar coupling. Using a combination of analytical derivations and numerical simulations, we explore the impact of interatomic distance, lattice symmetry, and external magnetic fields on quantum coherence. The study extends previous one-dimensional investigations to two-dimensional square, triangular, and hexagonal Ti-spin structures on an MgO substrate, where spin interactions can be manipulated at the atomic scale using scanning tunneling microscopy (STM). We analyse the eigenenergies and eigenstates of these systems and employ the Lindblad master equation to model decoherence processes. Our results show a competition between the Heisenberg exchange and the dipole-dipole coupling, with special attention to the intermediate regime. Additionally, we characterise spin relaxation and flipping dynamics, highlighting their dependence on structural variations. These insights contribute to the broader understanding of spin coherence in engineered quantum systems and provide a foundation for future experimental and theoretical studies in quantum nanoscience.

# Contents

# Chapter 1

# Introduction

The word 'atom' dates back to the ancient Greeks and means: an indivisible unit or the smallest building block of matter. This concept has changed over time. Since the late 19th century, physicists have discovered smaller particles, leading to the Standard Model in the 1980s. The current model includes six quarks (which make up protons, neutrons, and other hadronic particles), six leptons (the electron, muon, tau, and their corresponding neutrinos) and force-carrying particles (the gluon, photon, and graviton) along with the Higgs boson [1]. Although the original Greek model was replaced, the concept of the atom as the smallest building block still holds some truth, since up to this day, the atom remains the smallest unit that humans can use to construct materials.

In this thesis, we study theoretically two-dimensional structures atom by atom and seek to answer the following questions: How do quantum systems evolve in two-dimensional spin-$\frac{1}{2}$ lattices under varying magnetic fields and interatomic distances? What role does symmetry in two-dimensional structures play in spin decoherence when the quantum system is in contact with a surface serving as an infinite reservoir?

(a) (b)

Figure 1.1: Diagrams that show neighbouring atoms which experience both Heisenberg exchange coupling $J$ and dipole-dipole coupling $D$, which are represented by interactions between all atoms in the lattice. The atoms are coupled by a surface coupling $J_{\mathrm{surf}}$ and experience an applied magnetic field $\mathbf{B}$. (a) Square lattice of atoms aligned in a ferromagnetic configuration. (b) Hexagonal lattice of atoms aligned in a ferromagnetic configuration.

The OtteLab, which is part of the Department of Quantum Nanoscience at Delft University of Technology, assembles two-dimensional structures where they place atoms one-by-one on a surface and study the behaviour of the collective system using scanning tunneling microscopy (STM) (Figure 1.2a) [2]. STM is a form of microscopy developed by Gerd Binnig and Heinrich Rohrer at IBM Zürich, leading to a Nobel Prize in 1986 [3]. STM uses a sharp probe to scan surfaces at the atomic level, allowing for the manipulation and measurement of individual atoms (Figure 1.2b). In STM experiments, atoms can be positioned with subatomic precision by controlling the tunneling current between the tip and surface, a technique developed by Donald Eigler and Erhard Schweizer in 1990 [4]. Ti atoms, for instance, are positioned on a surface of MgO using controlled voltage pulses. Since then, STM has been expanded with methods such as spin-polarised STM (SP-STM), which measures magnetization using conductance changes, and inelastic electron tunneling spectroscopy (IETS), which provides information about an atom's energy levels. These methods have been used, among others, in experiments by Spinelli et al. to investigate the magnetic properties of spin waves in chains of magnetic atoms [5].

(a) (b)

Figure 1.2: (a) STM image showing the construction of atomic structures of Fe on $Cu_2N/Cu(100)$ on a 30 nm scale. (b) Illustration of STM scanning a surface at atomic resolution. Source: OtteLab [2].

In 2015, Baumann et al. modified the STM to include electron spin resonance (ESR), creating ESR-STM. This method allows for local spin manipulation with high spatial and energy resolution while reducing the effects of thermal broadening. Another technique, pump-probe spectroscopy, tracks time evolution by initializing a spin with a pump pulse and measuring its magnetization at a later time. The combination of these methods has been used by Veldman et al. to study the dynamics of coupled spins [6].
The interaction of quantum spins with their surroundings leads to relaxation and decoherence, which refers to the loss of coherence and entanglement due to interactions with surrounding particles. This is a key challenge in developing quantum devices and also sets the sensitivity limits for various magnetometry techniques. These effects are particularly relevant for spin-based quantum computing, including implementations using donors in silicon, electrons in quantum dots, and molecular magnets. Additionally, decoherence plays a role in the transition from quantum to classical behaviour [7]. To quantitatively describe decoherence, we employ the Lindblad master equation, a widely used formalism for modeling open quantum systems interacting with an environment [8].

In 2020, R. Broekhoven studied the flip-flop evolution of a well-tuned Ti dimer, where two adatoms' spins evolve together, in his Master's thesis. This experiment aimed to demonstrate undriven coherent evolution of a Ti dimer using STM. In 2023, M. Piek continued this work in her Bachelor's thesis by studying the decoherence and dynamics of spin chains of different lengths, coupled to an electron bath.
This thesis aims to extend the study from one-dimensional spin chains to two-dimensional structures, focusing on the quantum states and dynamics of square and hexagonal Ti-spin systems on an MgO lattice. We examine these states as a function of interatomic distances. In spin systems, interactions can be categorised into exchange coupling, which dominates at short distances due to wavefunction overlap, and dipolar coupling, which becomes more significant at larger separations. The competition between these interactions influences the stability and coherence of quantum states, making them important factors in spin-based quantum technologies. Additionally, we vary the applied magnetic field from a regime where it is dominant over coupling and temperature to one where it is nearly absent. Finally, we explore structural variations related to spin flipping, particularly for the hexagonal lattice.
The report is structured as follows: first, we discuss the experimental techniques, which have been briefly mentioned so far, in more detail (Chapter 2). Next, the system Hamiltonian for two-dimensional structures is introduced, including its coupling to the environment (Chapter 3). Chapter 4 examines the system in the context of the Lindblad equation, leading up to the numerical models and results presented in Chapter 5. Finally, conclusions and discussion are provided in Chapter 6.

# Chapter 2

# Experimental Techniques

In this chapter, we explore the experimental techniques used to measure and manipulate atomic spins on surfaces. This chapter serves as an experimental context for the remainder of this thesis, which will focus on the numerical analysis of quantum structures. We begin with an introduction to scanning tunneling microscopy (Sec. 2.1), which serves as a fundamental tool for the subsequent techniques. This method enables us to displace atoms (Sec. 2.3), identify their electronic and vibrational properties (Sec. 2.4), polarise spins (Sec. 2.5), and investigate spin interactions, including coupling and decay dynamics (Secs. 2.6 and 2.7).

## 2.1 Scanning Tunneling Microscopy

Microscopy is the technical field that uses microscopes to see objects invisible to the naked eye. Traditional microscopes enlarge an image of an object by scattering and refocusing light. This limits the size of the object due to the defraction limit. Electron microscopy overcomes this problem, since it does not use light but electrons to create an image. The object's resolution is now limited by the electron's wavelength, which can be as low as 0.1 nm and can be determined with the Broglie equation [9].

Scanning tunneling microscopy (STM) applies, as the name suggests, electron tunneling for surface shape detection [3]. Tunneling is a quantum mechanical phenomenon where particles enter areas which are classically forbidden due energy potential barriers, and reappear across the barrier. For STM the barrier concerns a narrow (few Ångstroms) vacuum between a probe and the surface. Electron tunneling causes a current to flow between the probe and the surface, which decays exponentially with distance as the tunneling probability decreases. For the current to remain constant, a feedback loop regulates the probe placement, which can be adjusted in distance from the surface and around the sample by a piezotube. Surface topographies are performed in constant-current mode.

## 2.2 Sample Preparation

All experiments regarding measurements and manipulation of atomic spins in the OtteLab are performed with the Unisoku USM-1300 $^3$He low temperature STM (Figure 2.1). This apparatus has a vector magnetic field of 9.0 T out-of-plane and 2.0 T in-plane and a base temperature of 330 mK due to $^3He$-cooling, which can be maintained for ±24 hours [2].

To perform experiments on atomic spins using the STM, one must prepare a surface by evaporating Ti and Fe atoms onto bilayer MgO islands grown on an Ag(100) crystal, following the method introduced by Yang et al. [10]. To obtain a clean Ag surface, it is first sputtered with ionised and accelerated Ar gas, where $Ar^+$ ions collide with the sample and remove surface contaminants. The surface is then annealed in a UHV chamber at 650˚C, allowing it to reconstruct into atomically flat Ag terraces. The bilayer MgO islands are grown by evaporating Mg atoms onto the sample in a low pressure $O_2$ atmosphere while maintaining a temperature of 400˚C. Finally, the sample is cooled to 1.5K for single atom deposition. At this stage, the sample is briefly removed from the STM, exposing it to a controlled flow of Fe and Ti atoms for approximately 30 seconds, before immediately returning it to the cryogenic environment [11].

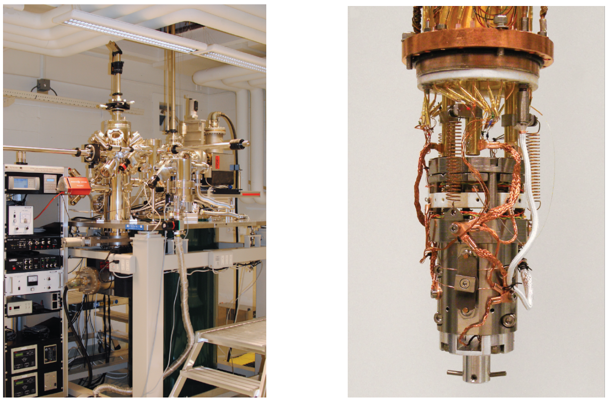

(a) (b)

Figure 2.1: (a) Picture of the Unisoku USM-1300 $^3He$ STM in Delft. (b) Picture of the scanning tunneling microscope taken during installation. Source: Spinelli et al.[5]

## 2.3 Atom Manipulation

In Section 2.1 the STM probe was shown to be able to detect its proximity to the surface. Besides imaging the surface topography, this property can be further exploited by letting it interact with the atoms on the surface. Once the tip of the probe approaches an atom on the surface, the additional Van der Waals force between the tip and the atom creates a combined potential well of the tip and surface. This attraction allows the probe to drag the atom around the surface and eventually place the atom by moving away from the surface: a process known as lateral manipulation [12].

### 2.3.1 Vertical Manipulation

Lateral manipulation however, is only possible for atoms that are bound loosely to the surface, depending on the surface lattice configuration. When this is not the case, instead of dragging, the atom has to be picked up such that the atom jumps on the STM probe, known as vertical manipulation. Initially, the procedure is the same as lateral manipulation, resulting in an asymmetric double potential well with a global minimum near the surface, where the atom is located. However, when further approaching the surface one can apply a negative voltage to the tip, distorting the double potential well so that the potential well of the tip is now the global minimum. The atom is displaced with the global minimum, so when the tip is lifted again, the atom will follow the larger potential well of the tip and is lifted [13]. In reverse, this procedure, with opposite tip charge, will drop the atom at a selected location.

During vertical manipulation of an atom, its magnetic moment polarises the probe tip, which can be effectively employed to measure the spins of surface atoms as discussed in Section 2.5.

## 2.4 Inelastic Electron tunneling Spectroscopy

The majority of tunneling in an STM is an elastic tunneling process, where the electron tunneling from sample to probe neither gains nor loses energy. However, occasionally electrons scatter, which gives rise to additional tunneling paths: inelastic tunneling. In Inelastic Electron Tunneling Spectroscopy (IETS) [14], a bias voltage is applied between the STM tip and the surface. If the voltage exceeds the electron's excitation energy, an electron can tunnel from atom to the tip. Consequently the tunneling current is measured as a function of the applied voltage. Electron tunneling leads to small steps in the tunneling current as a function of voltage that indicate the occurrence of inelastic tunneling events, which directly relates to the atom's energy level spectrum. Since every atom has a unique spectrum, IETS can be used to characterise atoms on a surface.

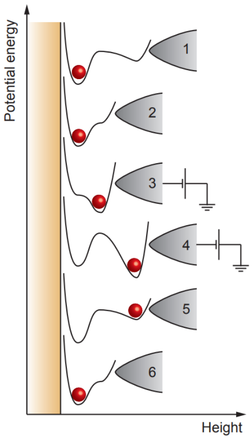

Figure 2.2: Visualisation of atom lifting and placing procedures for vertical atom manipulation. In all drawings, the left side of the double potential well represents the surface, the right side the tip. In (1) the tip is at constant-current distance for STM topography: the magnetic atom (red sphere) is stable on the surface. If the tip gets closer, the potential well is distorted (2). The atom is positively charged, so applying a negative tip bias causes the right side of the potential well to become a global minimum and the atom falls in (3). When the tip is then pulled away, the atom will move with it (4). After restoring the imaging settings (5), the atom will stay on the tip side. When the tip is then moved closer to the surface, the atom will easily fall back to the surface potential well(6). Source: Spinelli et al.[5]

## 2.5 Spin-Polarised STM

In addition to surface topography, STM is also able to observe the surface atom spin. One applies the vertical manipulation from Section 2.3.1 to pick up the atom and measure the tunneling current. This current is affected by tip-sample conduction which is again dependent on the overlap of the density of states of the tip relative to the surface atom of the sample [15]. When the polarisation of the tip and the substrate aligns, this overlap is larger and supports a larger current flow (Figure 2.3). This can be used to read out the spin of single magnetic atoms.

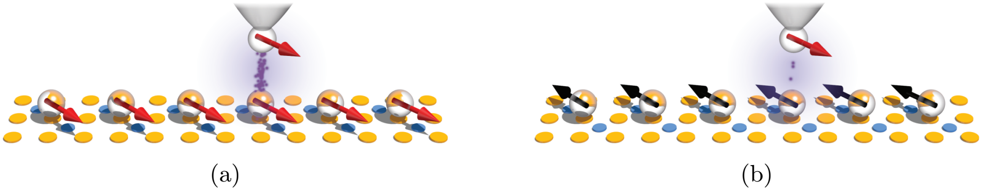
(a) (b)

Figure 2.3: Schematic of a spin-polarised tip reading a ferromagnetic structure. The tip hovers above a single magnetic atom. If the spin of this tip atom and the atom on the surface are in parallel (a) or antiparallel (b) alignment, the tunnel current will be higher (a) or lower (b). This structure itself is different from the structure used in this research. Source: Spinelli et al.[5]

In addition to the elastic part of the current, there exists an additional effect on the inelastic tunneling current in Section 2.4. The inelastic current depends on the sign of the bias voltage, resulting in asymmetric differential conductance steps. The amount of asymmetry is directly proportional to the polarisation of the STM tip, because each polarisation favours a particular spin excitation ($\Delta\sigma = \pm 1$). An excitation in the ground state always has $\Delta\sigma = 1$ and results in a larger tunneling current.

## 2.6 Electron Spin Resonance

We now consider the so called Zeeman effect. Electron spin gives rise to a magnetic moment with two possible orientations: spin-up ($+\frac{1}{2}$) and spin-down ($-\frac{1}{2}$). An external magnetic field causes the two spin states to split into states with different energy levels proportional to the strength of the magnetic field, known as Zeeman splitting. The method of electron Spin Resonance (ESR) applies microwave radiation to the sample. The resulting oscillating electric field is locally converted into an oscillating magnetic field, felt only by the atom directly underneath the tip. If the oscillating magnetic field matches the Larmor frequency of the atom, the atom experiences a Rabi rotation, resulting in a change in the spin-polarised conductance visualised in Figure 2.4 [6].

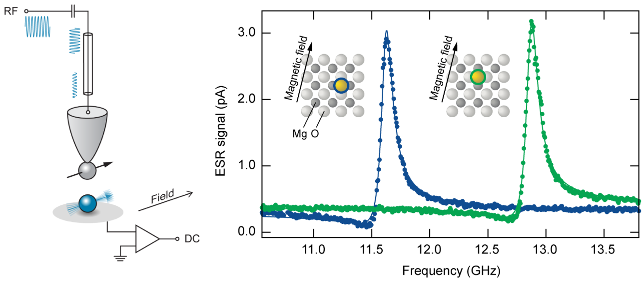

Figure 2.4: ESR measurement of a Ti atom on an MgO lattice structure located at two different bonding sites [2]. On the left, the radio frequency signal causes a Rabi rotation of the atom via the STM tip. On the right, the energy peaks belonging to the different bonding sites are presented.

The ESR signal can be used to measure the properties of the atom on the surface, such as the coupling strength, which is discussed in Section 3.1.2.

## 2.7 Pump-Probe Spectroscopy

Pump-probe spectroscopy is an efficient method to determine the relaxation time $T_1$ of the system [16]. Let us start with the components, which are two short DC voltage pulses.

- **Pump Pulse**
  This is the first pulse, which excites the atom from its ground state to a higher energy state.
- **Probe Pulse**
  After a controllable delay, a second pulse, called the probe, is sent to measure the state of the system by a spin-polarised current.

In our situation, we want to observe how quickly an atom relaxes to the ground state after being excited by the electric pump pulse. After the pump pulse, there is a period of rest, allowing the system to evolve over time. During this period, for example, an excited electron may relax back to its ground state or vibrational energy may dissipate through molecular motion. One prepares a set of measurements with different evolution times. After each period of time, one measures the state of the system by a spin-polarised current as in Section 2.5. The resulting data reveal the time evolution of the coherence evolution.

# Chapter 3

# Theory

The magnetic ordering in a material is determined by the spins of its atoms. We will discuss two categories magnetic ordering: ferromagnetic and antiferromagnetic (Figure 3.1). In both these materials, one atom's magnetisation direction determines all atoms' magnetisation directions. We describe the spin behaviour of particular atoms in a system using the spin Hamiltonian formalism, which we can tune for specific environments.

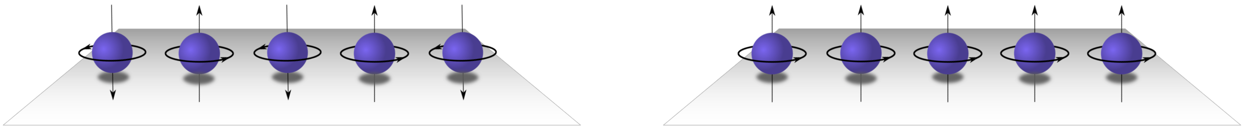

(a) Antiferromagnetic material

(b) Ferromagnetic material

Figure 3.1: Comparison between (a) antiferromagnetic and (b) ferromagnetic materials.

We can design the environments ourselves. Atom manipulation can create different structures of Ti atoms on the MgO lattice (Section 2.3.1). In one dimension, structure variation is limited to one axis, the choice of which does not affect the Hamiltonian in Section 3.1. Therefore, axes are left out for now until we expand the system to two dimensional structures in Section 3.2.

## 3.1 Hamiltonian

This research concerns the spin behaviour of atoms which are spin-$\frac{1}{2}$ particles: Ti atoms on a bilayer MgO film on Ag(100). Ti atoms have 2 electrons in their $3d$ orbital. However, Ti atoms show affinity for H atoms, therefore once Ti atoms are placed on the MgO film, they will pair with a H atom, resulting in one remaining free electron in the $3d$ shell with spin-$\frac{1}{2}$ [10]. This is currently a controversial explanation.

We will start with a chain of N spin-$\frac{1}{2}$ particles that only interact with their direct neighbours for which the complete Hamiltonian is given by [17]:

$$\hat{H} = \mu_B g \sum_{i=1}^{N} \mathbf{B} \cdot \hat{\mathbf{S}}^{(i)} + J \sum_{i=1}^{N-1} \hat{\mathbf{S}}^{(i)} \cdot \hat{\mathbf{S}}^{(i+1)} + D_0 \sum_{i=1}^{N-1} \left( \hat{\mathbf{S}}^{(i)} \cdot \hat{\mathbf{S}}^{(i+1)} - 3 \left( \hat{\mathbf{S}}^{(i)} \cdot n \right) \left( \hat{\mathbf{S}}^{(i+1)} \cdot n \right) \right) \tag{3.1}$$

The first summation regards the Zeeman effect due to the external magnetic field $\mathbf{B}$ with the Bohr magneton $\mu_B$ and the g-factor $g$ (Section 3.1.1). The second is the Heisenberg exchange coupling with coupling strength $J$ (this is covered in Section 3.1.2) and third the dipole-dipole coupling with dipolar coupling $D$ (this is covered in Section 3.1.3). These interactions with respect to spin in the atom chain are visualised in Figure 3.2.

### 3.1.1 Zeeman Interaction

Spin is an intrinsic form of angular momentum associated with a particle, and it interacts with an external magnetic field through the magnetic moment of the particle. This interaction leads to the splitting of energy levels, a phenomenon known as Zeeman splitting. Whenever a spin $\hat{\mathbf{S}}$ and a magnetic field $\hat{\mathbf{B}}$ are aligned, the energy level will decrease, whilst for anti-parallel alignment the energy level will increase. For a single particle the Zeeman Hamiltonian looks like:

$$\hat{H}_{\text{Z}} = \mu_B g \mathbf{B} \cdot \hat{\mathbf{S}}, \tag{3.2}$$

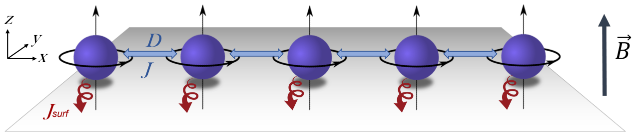

Figure 3.2: One dimensional chain of atoms aligned in ferromagnetic configuration, with an applied magnetic field $\mathbf{B}$. The neighbouring atoms experience Heisenberg exchange coupling and dipole-dipole coupling, visualised by $J$ and $D$ respectively. The choice of axis is arbitrary.

with the Bohr magneton $\mu_B$, the magnetic field $\mathbf{B}$ and the g-tensor $\mathbf{g}$. This is easily expanded to describe an entire chain of N particles as in equation (3.1). The Landé $g$-factor is a multiplicative term, depending on the site structure. For a free electron, it is a diagonal $3 \times 3$ matrix which reduces to $g_{xx} = g_{yy} = g_{zz} = 2.0023$. On the MgO lattice, the g-factor depends on the binding site. Forms of asymmetry in the surface lattice cause anisotropy in the $3 \times 3$ matrix. The result of the surface lattice and the effect on Zeeman splitting can be seen in Figure 3.3b.

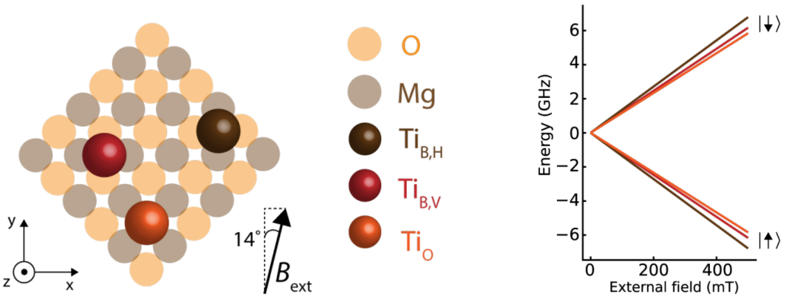

(a) (b)

Figure 3.3: Zeeman splitting and g-factor anisotropy. (a) Schematic image of Ti atoms bound on different binding site on the MgO lattice: located on the bridges are $Ti_{\mathrm{B,H}}$ horizontally and $Ti_{\mathrm{B,H}}$ vertically, located on the oxygen atom is $Ti_{\mathrm{O}}$. (b) Calculated Zeeman splitting for Ti on the three binding sites showing the effect of the difference in g-factor components. Source: Veldman et al.[11]

Besides the external magnetic field $B$, the STM probe tip also exerts a magnetic field $\mathbf{B}$ (Section 2.1), which is only relevant to the atom immediately underneath the tip, resulting in the following interaction Hamiltonian for the entire string:

$$\hat{H}_{\mathrm{tip}} = \mu_B g \mathbf{B}_{\mathrm{tip}} \cdot \hat{\mathbf{S}}, \tag{3.3}$$

resulting in the total Zeeman Hamiltonian:

$$\hat{H}_{\mathrm{Z}} = \mu_B g \sum_{i=1}^{N} \left( \mathbf{B} \cdot \hat{\mathbf{S}}^{(i)} \right) + \mu_B g \mathbf{B}_{\mathrm{tip}} \cdot \hat{\mathbf{S}}^{(i)}. \tag{3.4}$$

However, the Zeeman effect due to the magnetic field $\mathbf{B}_{\mathrm{tip}}$ is negligible compared to the external field $\mathbf{B}$, so the term is excluded from now on.

### 3.1.2 Heisenberg Exchange Coupling

In addition to interaction with the surrounding magnetic field, the atoms interact with each other and exchange spin information, hence the name exchange coupling. The outer electrons influence each other due to the overlap of their wavefunctions [18]. For atom $i$ and $i+1$ we obtain the following Hamiltonian:

$$\hat{H}_{\mathrm{Exc}} = J \hat{\mathbf{S}}^{(i)} \cdot \hat{\mathbf{S}}^{(i+1)}. \tag{3.5}$$

Here, $J$ is the coupling strength. The study by Yang et al. investigated the exchange interaction between Ti atoms on the MgO lattice [10]. Using STM, they precisely controlled the interatomic distance and orientation of Ti atoms, followed by ESR measurements to study the resulting spin states. Figure 2.4 shows the ESR spectrum, where two distinct peaks correspond to two bonding sites. When multiple Ti atoms are coupled, their ESR spectrum shows two peaks, which reflect the fact that the different spin states of an atom are coupled

to another at a specific distance. The peak separation, $\Delta f = (J + 2D)/\hbar$, enables the determination of the coupling constants.
The coupling parameter $J$ was found to follow the relation:

$$J = J_0 \exp\left[\frac{-(r - r_0)}{d_{ex}}\right], \tag{3.6}$$

where $r$ represents the interatomic distance, $r_0 = 8.64\text{Å}$ is the distance of three lattice constants, and $d_{ex} = 0.40 \pm 0.02\text{Å}$ is the characteristic decay length [10]. At $r_0$, $J_0 = 0.97 \pm 0.03$ GHz is the strength of the exchange coupling.
Due to exponential decay over distance (Figure 3.4c), we can disregard all interactions except direct neighbouring atoms. Furthermore, $J < 0$ for the antiferromagnetic coupling of the singlet state ($|-\rangle$), which results in lower energies, while $J > 0$ for the ferromagnetic coupling of the triplet states ($|\uparrow\uparrow\rangle$, $|\downarrow\downarrow\rangle$, $|+\rangle$), which results in higher energies. These shifts in energy due to exchange coupling are visualised in Figure 3.4b. For an N-particle chain this results in N interactions, resulting in the following Heisenberg exchange coupling term:

$$\hat{H}_{\text{Exc}} = J \sum_{i=1}^{N-1} \hat{\mathbf{S}}^{(i)} \cdot \hat{\mathbf{S}}^{(i+1)}. \tag{3.7}$$

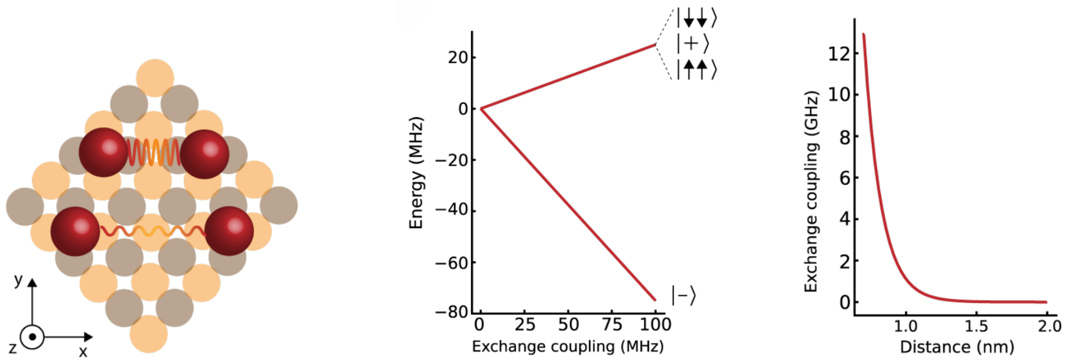

(a) (b) (c)

Figure 3.4: (a) Schematic picture of exchange coupled atoms on a surface at varying distances. (b) Energy diagram and eigenstates resulting from antiferromagnetic exchange coupling. (c) Characteristic exponential decay of exchange coupling over distance between two Ti atoms on a surface. Source:[11]

### 3.1.3 Dipole-Dipole Coupling

The Heisenberg coupling from the previous section is dominant at small distances. For large distances dipole-dipole coupling dominates. The atom spin creates a magnetic field, which is consequently felt by nearby atoms (Figure 3.5a). Dipolar coupling is different by nature from the exchange coupling. First, the decay is cubic and second, the coupling is anisotropic. We write dipole-dipole coupling as follows [19]:

$$\hat{H}_{\text{D}} = \frac{\mu_0 \gamma_i \gamma_{i+1} \hbar^2}{4\pi |\mathbf{r}_i|^3} \left[\hat{\mathbf{S}}^{(i)} \cdot \hat{\mathbf{S}}^{(i+1)} - 3\left(\hat{\mathbf{S}}^{(i)} \cdot \mathbf{n_i}\right)\left(\hat{\mathbf{S}}^{(i+1)} \cdot \mathbf{n_i}\right)\right]. \tag{3.8}$$

Here $\mathbf{r}_i$ is the vector between atom spin particle $(i)$ and $(i+1)$ and $|\mathbf{r}_i|$ is the distance separating them. $\mathbf{n_i}$ represents the unit vector of $\mathbf{r}_i$ and is equal to $\frac{\mathbf{r}_i}{|\mathbf{r}_i|}$. $\mu_0$ is the vacuum permeability, and $\gamma_i$ are the gyromagnetic ratios of the corresponding atoms, which we assume to be constant.

#### Secular Approximation

A common approach to apply the dipole-dipole coupling in recent research is the secular approximation, allowing us to simplify equation (3.8). For that we need the following definition: $\hat{\mathbf{S}}^{(i)} \cdot \hat{\mathbf{S}}^{(i+1)} = \hat{S}_x^{(i)} \hat{S}_x^{(i+1)} + \hat{S}_y^{(i)} \hat{S}_y^{(i+1)} + \hat{S}_z^{(i)} \hat{S}_z^{(i+1)}$, and $S_x = \frac{1}{2}(\hat{S}^+ + \hat{S}^-)$ and $S_y = \frac{1}{2i}(\hat{S}^+ - \hat{S}^-)$. Moreover, we introduse $D_0 = \frac{\mu_0 \gamma_i \gamma_{i+1} \hbar^2}{4\pi |\mathbf{r_i}|^3}$ and here we assume that $\gamma_i$ is the same for all atoms. Besides, we present $n_i$ in spherical coordinates:

$$\mathbf{n}_i = \begin{bmatrix} \cos\phi\sin\theta \\ \sin\phi\sin\theta \\ \cos\theta \end{bmatrix}, \tag{3.9}$$

which can be substituted in equation (3.8). Regrouping the terms results in:

$$\begin{aligned} \hat{H}_\mathrm{D} =& D_0 \Bigg[ \left(1-3\cos^2\theta\right) \left( \hat{S}_z^{(i)}\hat{S}_z^{(i+1)} - \frac{1}{4}\left( \hat{S}^{(i)+}\hat{S}^{(i+1)-} + \hat{S}^{(i)-}\hat{S}^{(i+1)+} \right) \right) - \\ & \frac{3}{2}\cos\theta\sin\theta \left( \left( \hat{S}^{(i)+}\hat{S}_z^{(i+1)} + \hat{S}_z^{(i)}\hat{S}^{(i+1)+} \right) e^{-i\phi} + \left( \hat{S}^{(i)-}\hat{S}_z^{(i+1)} + \hat{S}_z^{(i)}\hat{S}^{(i+1)-} \right) e^{i\phi} \right) - \\ & \frac{3}{4}\sin^2\theta \left( \hat{S}^{(i)+}\hat{S}^{(i+1)+}e^{-2i\phi} + \hat{S}^{(i)-}\hat{S}^{(i+1)-}e^{2i\phi} \right) \Bigg]. \end{aligned} \tag{3.10}$$

Assuming $E_\mathrm{Zeeman} > E_\mathrm{Dipole}$, we apply the secular approximation [19], which assumes that only the terms that commute with the Zeeman Hamiltonian (which is proportional to $\sum \hat{S}_z$) are preserved. A strong applied magnetic field in the z-direction forces the spins to align along the z-axis. This means that terms involving $\hat{S}_x\hat{S}_y$, $\hat{S}_x\hat{S}_z$ and $\hat{S}_y\hat{S}_z$ in equation (3.10) can be discarded because they oscillate rapidly in the rotating frame and average to zero. The dipole coupling Hamiltonian becomes:

$$\begin{aligned} \hat{H}_\mathrm{D} &= D_0\left(1-3\cos^2\theta\right)\left[ \hat{S}_z^{(i)}\hat{S}_z^{(i+1)} - \frac{1}{4}\left( \hat{S}^{(i)+}\hat{S}^{(i+1)-} + \hat{S}^{(i)-}\hat{S}^{(i+1)+} \right) \right] \\ &= \frac{D_0}{2}\left(1-3\cos^2\theta\right)\left[ 2\hat{S}_z^{(i)}\hat{S}_z^{(i+1)} - \hat{S}_x^{(i)}\hat{S}_x^{(i+1)} - \hat{S}_y^{(i)}\hat{S}_y^{(i+1)} \right] \\ &= D\left[ 2\hat{S}_z^{(i)}\hat{S}_z^{(i+1)} - \hat{S}_x^{(i)}\hat{S}_x^{(i+1)} - \hat{S}_y^{(i)}\hat{S}_y^{(i+1)} \right], \end{aligned} \tag{3.11}$$

with $D = \frac{D_0}{2}(1-3\cos^2\theta)$. Here, $\theta$ represents the angle between the magnetic field $\mathbf{B}$ and the orientation of the atom pair. Consequently, the angle determines whether the dipolar coupling is weakly ferromagnetic or strongly antiferromagnetic. Moreover, at certain angles (54.7° and 125.3°) there is no dipolar coupling at all, which can be seen in Figure 3.5b.

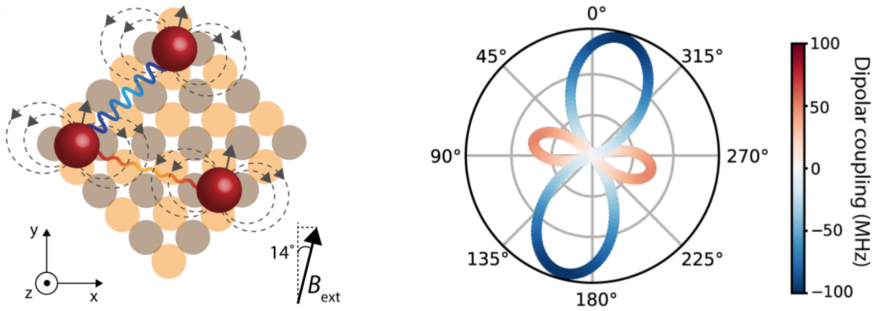

(a)

(b)

Figure 3.5: (a) Schematic picture of Ti atoms on a MgO surface and the magnetic field lines emanating from them. Depending on their relative orientation, the dipolar coupling can be ferromagnetic or antiferromagnetic. (b) Angle dependence of the dipolar coupling parameter D calculated for constant distance $|r|$. The external field is applied at a 14° angle. The radial axis of the plot shows the absolute value of the dipolar constant $|D|$ while the colour also shows the sign of the coupling. Source:[11]

To conclude, we have approximated the dipole-dipole coupling, which for a string of N particles becomes:

$$\hat{H}_\mathrm{D} = D\sum_{i=1}^{N-1}\left[ 2\hat{S}_z^{(i)}\hat{S}_z^{(i+1)} - \hat{S}_x^{(i)}\hat{S}_x^{(i+1)} - \hat{S}_y^{(i)}\hat{S}_y^{(i+1)} \right]. \tag{3.12}$$

This research will focus on two-dimensional structures. In contrast to the one-dimensional structure, it is now necessary to define all axes of the three-dimensional space. In combination with the secular approximation, which uses the angle of the plane with respect to the applied field, the results for the two-dimensional structures are strongly dependent on the structure orientation. For simplicity and accuracy, we do not use the secular approximation and use the Hamiltonian above in equation (3.8) instead. For that, we sum equation (3.8) over N atoms:

$$\hat{H}_{\mathrm{D}} = D_0 \sum_{i=1}^{N-1} \left[ \hat{\mathbf{S}}^{(i)} \cdot \hat{\mathbf{S}}^{(i+1)} - 3 \left( \hat{\mathbf{S}}^{(i)} \cdot \mathbf{n_i} \right) \left( \hat{\mathbf{S}}^{(i+1)} \cdot \mathbf{n_i} \right) \right]. \tag{3.13}$$

### 3.1.4 Hyperfine Coupling

This research is applied to $^{48}Ti$ atoms. These have 74% abundance and a net-0 nuclear spin. However, recent experiments have also considered its two isotopes: $^{47}Ti$ and $^{49}Ti$ with net nuclear spin $\frac{5}{2}$ and $\frac{7}{2}$ respectively. As we have discussed so far for electron spin, the nuclear spin in this case will create its own small magnetic field. Hyperfine coupling is the interaction between this magnetic field and the one emanating from the electron spin in the atom [11]:

$$\hat{H}_{\mathrm{hf}} = \hat{\mathbf{I}} \cdot \mathbf{A} \cdot \hat{\mathbf{S}}, \tag{3.14}$$

with nuclear spin $\hat{\mathbf{I}}$, coupling tensor $\mathbf{A}$ between the nuclear and electron spin, and the electron spin $\hat{\mathbf{S}}$. This is easily generalised for an N-particle system:

$$\hat{H}_{\mathrm{hf}} = \sum_{i=1}^{N} \left( \hat{\mathbf{I}}^{(i)} \cdot \mathbf{A} \cdot \hat{\mathbf{S}}^{(i)} \right). \tag{3.15}$$

This research covers $^{48}Ti$ only and therefore the hyperfine coupling is not incorporated in equation (3.1).

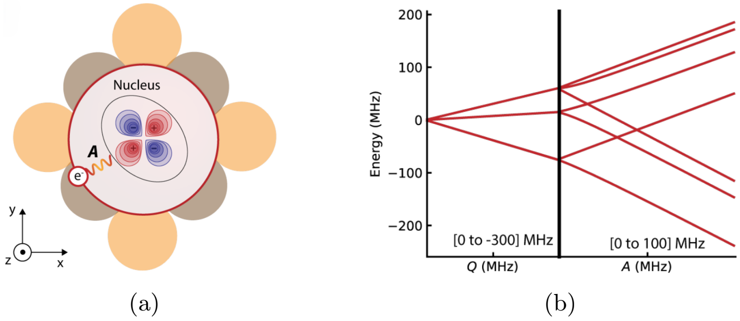

(a) (b)

Figure 3.6: (a) Schematic picture of the interactions between nuclear and electronic spins inside a single Ti atom. The nuclear quadrupole charge distribution is approximated by an ellipsoid. (b) Calculations of the energy level splitting due to quadrupole and hyperfine interactions. Calculations were done using $\eta = 0$, $I = \frac{5}{2}$ and $S = \frac{1}{2}$. Source:[11]

## 3.2 Two Dimensional Lattice

Up until this point, we have discussed a 1D chain of N atoms resulting in the Hamiltonian given in equation (3.1). Let us now consider a two dimensional structure on the $xy$-plane. There are infinitely many options, but we will limit this research to a square and triangular structure, where we consider a number of 4 and 7 atoms respectively. In contrast to the nearest-neighbour approximation for the one dimensional string of atoms, we will extend this model to all atom-atom combinations within the lattice. Consequently, the atoms are now identified by individual numbers instead of their lattice coordinates. Still, a nearest neighbour approximation for the two dimensional square and triangular lattice is presented in Appendix A.2.

The MgO surface on which we place the Ti atoms plays a significant role, because the Ti atoms cannot be placed anywhere on the surface (Figure 3.7). Placement sites for Ti atoms are the two different oxygen bridges and on top of the oxygen atom itself. As discussed in Section 3.1.1, these different sites lead to different g-factors for the Zeeman interaction. An important result is that for the triangular structure, the MgO square lattice determines the exact angles and distances between the Ti atoms, which on their turn determine the Hamiltonian.

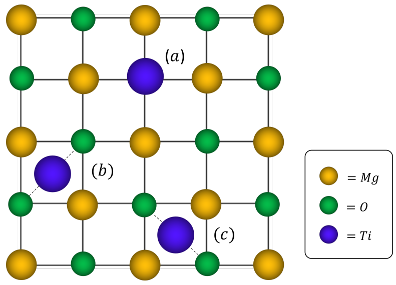

Figure 3.7: Illustration of a lattice structure with yellow Mg-atoms and green O-atoms. The lattice highlights two diagonal bridges formed by O atoms: (b) one extending from the lower left to the upper right and (c) the other from the upper left to the lower right. Blue Ti-atoms are shown, which can occupy three distinct sites: along the two O-O diagonal bridges or directly on top of an O atom (a). This configuration illustrates the possible Ti positions within the lattice framework.

### 3.2.1 Square Lattice

For the square lattice we consider the structure shown in Figure 3.8 with $A = 4$ and individual atom numbering. Similar to Section 3.1, we will build the Hamiltonian by summing the Zeeman interaction, the Heisenberg exchange, the dipole-dipole coupling, and the hyperfine coupling.

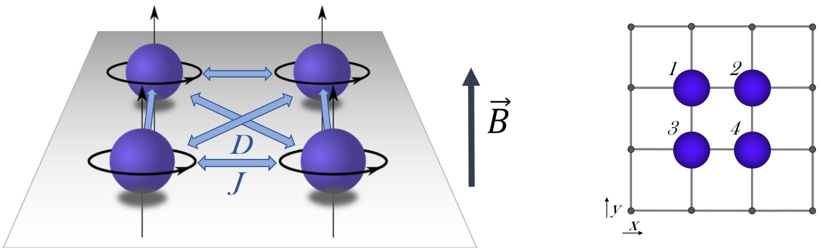

(a) Frontal view

(b) Top view

Figure 3.8: Example of a two-dimensional square lattice of atoms aligned in a ferromagnetic configuration with an applied magnetic field **B**. (a) Diagram that shows atoms which experience both Heisenberg exchange coupling $J$ and dipole-dipole coupling $D$, which are represented by interactions between all atoms in the lattice. (b) Top view, denoting lattice axes and atom numbering.

### Zeeman Interaction

We described the Zeeman interaction for the one dimensional chain in Section 3.1.1. Because it is a single-particle effect, this equation is easily adapted for the square lattice in Figure 3.8. We define $A$ as the set of all atoms $(a)$, so that the Zeeman interaction becomes:

$$\hat{H}_{\mathrm{Z}} = \mu_B g \sum_{a \in A} \mathbf{B} \cdot \hat{\mathbf{S}}^{(a)}. \tag{3.16}$$

### Heisenberg Exchange Coupling

Let us continue with the set of atoms $A$, where we now consider the Hamiltonian for the Heisenberg exchange coupling between all atoms in set $A$:

$$\hat{H}_{\mathrm{Exc}} = J \sum_{\substack{a,b \in A \\ a \neq b}} \hat{\mathbf{S}}^{(a)} \cdot \hat{\mathbf{S}}^{(b)}. \tag{3.17}$$

### Dipole-Dipole Coupling

As a result of equation (3.13) from Section 3.1.3, the Hamiltonian for dipolar coupling becomes:

$$\hat{H}_{\mathrm{D}} = D_0 \sum_{\substack{a,b \in A \\ a \neq b}} \left[ \hat{\mathbf{S}}^{(a)} \cdot \hat{\mathbf{S}}^{(b)} - 3 \left( \hat{\mathbf{S}}^{(a)} \cdot \mathbf{n}_{ab} \right) \left( \hat{\mathbf{S}}^{(b)} \cdot \mathbf{n}_{ab} \right) \right]. \tag{3.18}$$

Here $\mathbf{b}_{ab}$ represents the unit vector of $\mathbf{r}_{ab}$, the vector between atom spin particle $(a)$ and $(b)$, and is equal to $\frac{\mathbf{r}_{ab}}{|\mathbf{r}_{ab}|}$.

### Square Lattice Hamiltonian

The sum of the Zeeman, exchange and dipole Hamiltonian for the square lattice of atom set $A$ is:

$$\hat{H}_{\mathrm{2D}} = \mu_B g \sum_{a \in A} \mathbf{B} \cdot \hat{\mathbf{S}}^{(a)} + \sum_{\substack{a,b \in A \\ a \neq b}} \left[ (J + D_0)\, \hat{\mathbf{S}}^{(a)} \cdot \hat{\mathbf{S}}^{(b)} - 3D_0 \left( \hat{\mathbf{S}}^{(a)} \cdot \mathbf{n}_{ab} \right) \left( \hat{\mathbf{S}}^{(b)} \cdot \mathbf{n}_{ab} \right) \right]. \tag{3.19}$$

## 3.2.2 Triangular Lattice

A more interesting structure than the square lattice is the triangular lattice. Whereas in a square lattice the system's energy can be minimised by an antiferromagnetic configuration, this is impossible in a triangle. Once two out of three spins are opposite, the third can no longer orient itself opposite to both. The geometry of the lattice is incompatible with the interactions favoured by the system, which is called geometrical frustration [20]. The Kagome lattice is a more complicated structure which also results in frustratino. We can model it on a triangular lattice as a hexagon of six spins, with a seventh spin in the centre, illustrated in Figure 3.9. It follows the same atomic numbering in the $xy$-plane as the square lattice. The inter-atomic interactions are only depicted for atom number 1 for the sake of clarity. The Zeeman interaction and couplings are only briefly noted, because they remain the same as in the square lattice, except for the summation terms, which we specify for a hexagonal configuration of size $|B| = 7$, with $B$ the set of all atoms.

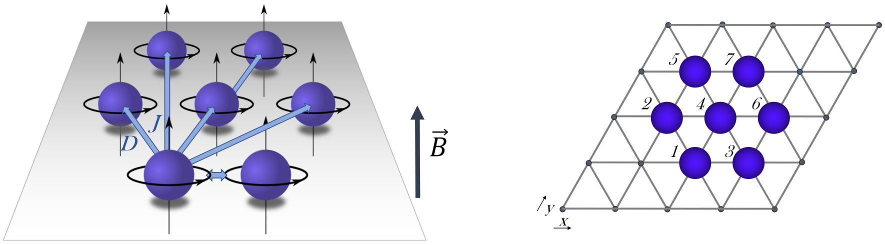

(a) Frontal view (b) Top view

Figure 3.9: Hexagon in a two-dimensional triangular lattice of atoms aligned in a ferromagnetic configuration with an applied magnetic field **B**. a) Simplified diagram where only atom number 1 experiences both Heisenberg exchange coupling $J$ and dipole-dipole coupling $D$. The interactions are visualised between all atom pairs in the lattice for atom 1. b) Top view, denoting lattice axes and atom numbering.

Although the MgO lattice is an exact square lattice, with fixed atomic positions as shown in Figure 3.7, we can only approximate a hexagonal arrangement of the atoms on this lattice. An example is given in Figure 3.10, with interaction angles of $\theta_1 = \arctan\frac{2}{1} \approx 63°$ and $\theta_2 = \arctan\frac{2}{-1} \approx 117°$. Throughout this research, we will use various compositions to study the hexagon at various interatomic distances and placement sites, where greater distances also allow for a better hexagonal approximation in the square lattice.

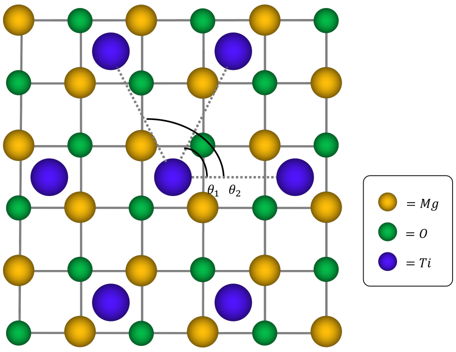

Figure 3.10: Approximate hexagonal configuration on a square lattice, showing the interaction angles $\theta_1 = \arctan\frac{2}{1}$ and $\theta_2 = \arctan\frac{2}{-1}$

### Triangular Lattice Hamiltonian

The Hamiltonian for the square lattice in equation (3.19) is defined such that it can be applied to any two-dimensional structure. Therefore, the complete Hamiltonian for the hexagonal configuration on a square lattice can be defined similarly, now for atom set $B$:

$$\hat{H}_{2\mathrm{D}} = \mu_B g \sum_{a \in B} \mathbf{B} \cdot \hat{\mathbf{S}}^{(a)} + \sum_{\substack{a,b \in B \\ a \neq b}} \left[ (J + D_0)\, \hat{\mathbf{S}}^{(a)} \cdot \hat{\mathbf{S}}^{(b)} - 3D_0 \left( \hat{\mathbf{S}}^{(a)} \cdot \mathbf{n}_{ab} \right) \left( \hat{\mathbf{S}}^{(b)} \cdot \mathbf{n}_{ab} \right) \right]. \tag{3.20}$$

## 3.3 Decoherence

So far, we have discussed various interactions between the system and its environment, as well as the interactions within the system itself. In the idealised case of a single atom with no external magnetic field or influence from the tip, the system approaches that of an isolated atom. In this scenario, without any external perturbations, the atom remains in a fixed quantum state. If there exists a well-defined phase relationship between the components of a quantum superposition, the system is said to be in a coherent state. For an isolated system, this coherence is maintained indefinitely. However, in most cases, as we will explore in Section 3.4, the system is not isolated, and interactions with the environment cause entanglement, leading to the loss of information and dissipation of energy: a process known as decoherence. The characteristic time over which the system loses its coherence is represented by the decoherence, time $T_2$.

#### Relaxation Time

When a system is coupled to a significantly larger environment at a constant temperature, it tends to relax towards thermal equilibrium. This relaxation process involves the exchange of energy between the system and its environment, a form of decoherence that results in a transition between energy levels. The time it takes for the system to reach thermal equilibrium through energy dissipation is known as the relaxation time, $T_1$.

#### Pure Dephasing Time

Pure dephasing is a process that does not involve changes in the energy levels of the system, but rather the loss of phase coherence in a superposition state. This happens when there is no energy exchange between the system and the environment, but environmental fluctuations still introduce fluctuations in the phase of the quantum state, leading to destructive interference between the components of the superposition. These environmental fluctuations can be the result of electromagnetic noise, lattice vibrations, or spin/charge noise, and are completely random. Over time, this results in a loss of coherence, and the time for complete phase decoherence is referred to as the pure dephasing time, $T_\phi$.

These three timescales, decoherence time $T_2$, relaxation time $T_1$, and pure dephasing time $T_\phi$, are related by the Bloch-Redfield theory [7] as follows:

$$\frac{1}{T_2} = \frac{1}{2T_1} + \frac{1}{T_\phi}. \tag{3.21}$$

## 3.4 Transition Rates

With this foundation in decoherence processes, we can now dive into the mathematical formalism used to describe transition rates in the system. In the study by Loth et al., the interaction between atom electrons and surface electrons is incorporated into the Pauli rates [16]. The standard model for inelastic electron tunneling is used to describe the transition rate from the eigenstate of the system $|i\rangle$ to $|j\rangle$. The transition rate is given by:

$$r_{i\to j} = \frac{G_S}{e^2} P_{i\to j} \int_{-\infty}^{+\infty} f(E)\left[1 - f(E - E_j + E_i)\right] dE, \tag{3.22}$$

which simplifies to:

$$r_{i\to j} = \frac{G_S}{e^2} P_{i\to j} \frac{\epsilon_{ij}}{e^{\epsilon_{ij}/k_B T} - 1}, \quad \text{if } E_i \neq E_j, \tag{3.23}$$

$$r_{i\to j} = \frac{G_S}{e^2} P_{i\to j} k_B T, \quad \text{if } E_i = E_j. \tag{3.24}$$

Here, $f(E)$ represents the Fermi-Dirac distribution:

$$f(E) = \left(1 + e^{-E/k_B T}\right)^{-1}. \tag{3.25}$$

In these expressions, $E_i$ and $E_j$ are the eigenenergies of the initial and final states, respectively, while $\epsilon_{ij} = E_j - E_i$ denotes the energy difference between them. The prefactor $G_S$, the surface-atom-surface conductance, characterises the strength of spontaneous relaxation, which is governed by conduction through the thin insulating layer of MgO.

The transmission coefficients $P_{i\to j}$ describe the probability of spin scattering via the Kondo interaction per unit time. These coefficients are related to the quantum mechanical transition intensities by:

$$P_{i\to j} = \frac{1}{P_0} \sum_{\sigma_k, \sigma'_k} \left| \langle i\sigma_k | \hat{\sigma} \cdot \hat{S} | j\sigma'_k \rangle \right|^2. \tag{3.26}$$

In this equation, $\sigma_k$ and $\sigma'_k$ represent the initial and final spin states of the scattering electron, respectively, and $|i\sigma_k\rangle$ corresponds to the product state of the atom's spin and the scattering electron spin. $P_0$ is a normalization factor. The term $\hat{\sigma} \cdot \hat{S}$ in the transition probability formula is directly related to the exchange interaction in the Kondo Hamiltonian. Additionally, transitions where $i = j$ (that is, remaining in the same eigenstate) are included to account for pure dephasing. The result is [21]:

$$r_{i\to j} = \frac{\epsilon_{ij}}{e^{\epsilon_{ij}/k_B T} - 1} J^2_{\text{surf}} \sum_{\sigma_k, \sigma'_k} \left| \langle i\sigma_k | \hat{\sigma} \cdot \hat{S} | j\sigma'_k \rangle \right|^2, \quad \text{if } E_i \neq E_j, \tag{3.27}$$

$$r_{i\to j} = k_B T J_{\mathrm{surf}}^2 \sum_{\sigma_k, \sigma'_k} \left| \langle i\sigma_k | \hat{\sigma} \cdot \hat{S} | j\sigma'_k \rangle \right|^2, \quad \text{if } E_i = E_j. \tag{3.28}$$

The Kondo Hamiltonian $\hat{H}_{R-Q}$ defines the exchange interaction between the local spin $\hat{S}$ and the conduction electron spin $\hat{s}$. The conducting surface electrons in the s-orbit scatter off the unpaired d-orbital electrons from the Ti atoms [22]. This interaction causes the system to transition between different spin states. For magnetic atoms on a surface the Kondo exchange interaction Hamiltonian is [23]:

$$\hat{H}_{R-Q} = \sum_{a\in A, q} J_{(q)} \hat{S}_q^{(a)} \otimes \hat{s}_q^{(a)}. \tag{3.29}$$

with $a$ specifying the Ti atom, $J$ is the Kondo coupling strength and $q = (x, y, z)$. $\hat{S}^{(a)}$ is the spin projection and $\hat{s}^{(a)}$ is the surface spin projection density of atom $a$ in the atom structure $A$.

# Chapter 4

# Decoherence: Lindblad Equations

In the previous sections, we have seen various Hamiltonians describing the different interactions within the system. Hamiltonians are necessary to predict the future energy states of a quantum system, which is most famously done by applying the Schrödinger equation. However, to consider decoherence in a system, we can no longer use the wave function, but instead must use the density matrix. Therefore, a good alternative for the Schrödinger equation is the Lindblad equation [24]. In this section, we will first elaborate on density matrices and consequently discuss the derivation of the Lindblad equation and why we use it instead of the Schrödinger equation.

## 4.1 Density Matrices

Density matrices provide a framework for describing quantum systems that exist in statistical mixtures of states. Unlike the wavefunction formalism, which is primarily suited for pure states, the density matrix can capture both pure and mixed states, making it a practical tool in the study of quantum decoherence and decay processes. In such scenarios, a system can transition from a pure quantum state to a probabilistic mixture as a result of interactions with the environment. The density matrix is a specific representation of the density operator with respect to an orthonormal basis $\{|e_n\rangle\}$, in which each basis vector corresponds to a possible quantum state of the system [18]. The density operator is generally expressed as:

$$\hat{\rho} = \sum_{ij} p_{ij} \left| e_i \right\rangle \left\langle e_j \right|, \tag{4.1}$$

where $p_n$ represents the probability of the system being found in a given basis state $|e_n\rangle$.
The elements of the density matrix, denoted as $\rho_{ij}$, are obtained by projecting the density operator onto these basis states:

$$\rho_{ij} = \left\langle e_i \right| \hat{\rho} \left| e_j \right\rangle = \sum_n p_n \left\langle e_i | e_n \right\rangle \left\langle e_n | e_j \right\rangle. \tag{4.2}$$

A density matrix consists of two distinct types of elements:

- **Populations**: The diagonal elements $\rho_{ii}$ represent the probability of the system being found in the corresponding basis state $|e_i\rangle$.
- **Coherences**: The off-diagonal elements $\rho_{ij}$ (for $i \neq j$) quantify the degree to which the system exists in a superposition of different basis states.

To ensure that the density matrix represents a physically valid quantum state, it must satisfy certain mathematical properties. First, it must be **positive semidefinite**, which ensures that all its eigenvalues are non-negative. Consequently, the sum of all probabilities must equal one:

$$\sum_n p_n = 1, \quad \text{with } 0 \leq p_n \leq 1. \tag{4.3}$$

The distinction between pure and mixed states is also reflected in the trace of the density matrix. For a pure state, which consists of eigenstates and their superpositions, the matrix satisfies $\mathrm{Tr}(\rho^2) = 1$, while for a mixed state, where the system is described by a statistical ensemble, $\mathrm{Tr}(\rho^2) < 1$.
In addition to these conditions, a valid density matrix must adhere to two further properties:

- It is **Hermitian**, meaning $\rho = \rho^\dagger$, ensuring that all its eigenvalues are real.
- It is **idempotent** in the case of a pure state that satisfies $\rho^2 = \rho$.

The expectation value of an observable $\hat{A}$ in the state described by the density matrix is given by:

$$\langle A \rangle = \mathrm{Tr}(\rho \hat{A}) = \sum_{ij} \rho_{ij} \langle e_j | \hat{A} | e_j \rangle . \tag{4.4}$$

This expression reveals that the expectation value is a weighted average of possible measurement outcomes, where the weights correspond to the probabilities $p_i$.

## 4.2 Lindblad equation

Let us derive (partially) the Lindblad equation, also known as the master equation: terms that will be used interchangeably throughout this thesis. Reconsider what we have just discussed regarding the Schrödinger equation:

$$i\hbar \frac{\mathrm{d}}{\mathrm{d}t} |\psi(t)\rangle = \hat{H} |\psi(t)\rangle . \tag{4.5}$$

Here, we can substitute the density matrix, which results in:

$$\frac{\mathrm{d}}{\mathrm{d}t} \hat{\rho}(t) = -\frac{i}{\hbar} [\hat{H}, \hat{\rho}(t)]. \tag{4.6}$$

This is the von Neumann equation and describes the time evolution of a density matrix $\hat{\rho}$ with Hamiltonian $\hat{H}$. For isolated atoms, this equation would be simple enough to solve; nevertheless, this chapter has discussed the numerous environmental influences, and thus the resulting density matrix of the complete environment will be far too elaborate. Moreover, this effectively makes the von Neumann equation useless because we are merely looking for the density matrix of the system, not the environment. That is why we introduce the Liouvillian superoperator [8]:

$$\hat{L}_k \hat{\rho} \hat{L}_k^\dagger - \frac{1}{2} \hat{L}_k^\dagger \hat{L}_k \hat{\rho} - \frac{1}{2} \hat{\rho} \hat{L}_k^\dagger \hat{L}_k. \tag{4.7}$$

Here, $\hat{L}_k$ are jump operators that describe the effect of the coupling of the density matrix of the system $\hat{\rho}$ to the environment, which combined with an adjusted weight factor acts as decoherence. The corresponding jump operators are discussed in Section 4.3. Consequently, under assumptions we will discuss shortly, this results in the Lindblad equation also known as the master equation [24]:

$$\begin{aligned} \frac{\mathrm{d}}{\mathrm{d}t} \hat{\rho}(t) &= -\frac{i}{\hbar} [\hat{H}, \hat{\rho}(t)] + \sum_k \frac{1}{2} \left( 2\hat{L}_k \hat{\rho} \hat{L}_k^\dagger - \hat{L}_k^\dagger \hat{L}_k \hat{\rho} - \hat{\rho} \hat{L}_k^\dagger \hat{L}_k \right) \\ &= -\frac{i}{\hbar} [\hat{H}, \hat{\rho}(t)] + \sum_k \left( \hat{L}_k \hat{\rho} \hat{L}_k^\dagger - \frac{1}{2} \left\{ \hat{L}_k^\dagger \hat{L}_k, \hat{\rho} \right\} \right), \end{aligned} \tag{4.8}$$

where $\{A, B\} = AB + BA$ is the anticommutator.
Let us now talk about the aforementioned assumptions necessary to derive the master equation. There are three methods to derive the master equation [25]: the weak coupling limit, the low density limit, and the singular coupling limit, which will all result in the same master equation. A variety of these approximations is used for each of these methods. Hence we will now briefly go through these methods, but for the full derivation one can consult [24][8][25].

- **Second order perturbation**
  Recall our system of Ti atoms on a bilayer of MgO on an Ag surface. We consider the coupling between the system and its environment to be weak because of the insulating layer of MgO and therefore we may approximate the environment's effect on the system to be a small disturbance to the relatively stable system. That is when we can apply the second order perturbation theory on the system's evolution [18].
- **Born approximation**
  Due to a weak coupling between the system and its environment, the environment, which is supposed to be much larger than the system, will experience very little disturbance from the system. Therefore, the system should not alter the environment's eigenstates too much, so we can approximate the environment to be in thermal equilibrium. This initially bares great resemblance to the second-order perturbation, but now concerns the environment [26].

- **Markov approximation**
  A Markov process is a sequence of stochastic events where the probability of any event depends only on its current state, thus the result of the previous event: exactly what we need for the Lindblad equation. Without the Markov approximation the equation 'memorises' past interactions between the system and the environment, leading to complicated equations. The Markov approximation is allowed when the correlation time of the environment is much smaller than the integration time steps.
- **Strong secular approximation**
  The equation contains oscillating terms of the form $e^{i(\omega-\omega')t}$ that correspond to transitions between energy levels with frequencies $\omega$ and $\omega'$ of the system. Whenever $\omega \neq \omega'$, these frequencies are significantly high with respect to the system's evolution frequencies; thus, eventually these terms average out to zero over time. This implies that only terms where $\omega = \omega'$ remain, so different transition frequencies evolve independently and the evolution of populations with different energy levels is decoupled. As expected, this only works for systems with weak interactions [27].

The derivation of the Lindblad equation is reliant on time integration throughout these approximations. In order to integrate over time, the integration time steps must be smaller than the evolution time of the system's collective spin state.

## 4.3 Jump Operators

For the application of the master equation, jump operators $\hat{L}_k$ are used. Here, one can choose from operators in the spin eigenbasis or in the energy eigenbasis. The latter model explores the impact of the environment on the energy eigenstates of an entire chain. The environment interacts with the chain through a spin-scattering electron, which can be mathematically described by diagonalizing the Hamiltonian $H = PDP^\dagger$, where $D$ is a diagonal matrix containing the energy eigenvalues. This allows for the transformation between the spin eigenbasis ($\hat{\rho}_S$) and the energy eigenbasis ($\hat{\rho}_E$) through the relations: $\hat{\rho}_E = P^\dagger \hat{\rho}_S P$ and vice versa, $\hat{\rho}_S = P\hat{\rho}_E P^\dagger$. In the energy eigenbasis, the eigenstates correspond to standard basis vectors, and degenerate eigenstates are represented multiple times in $D$. Despite this degeneracy, distinct spin eigenstates remain distinct in the energy basis.
The eigenvectors are ordered from lowest to highest eigenvalue and follow this convention:

$$\begin{pmatrix}1\\0\\\vdots\\0\end{pmatrix}, \begin{pmatrix}0\\1\\\vdots\\0\end{pmatrix}, \dots, \begin{pmatrix}0\\\vdots\\0\\1\end{pmatrix}. \tag{4.9}$$

In this setup, the energy ladder operators are $2^N \times 2^N$ matrices (where $N$ is the number of particles, which implies a $2^N$-dimensional state space for spin-1/2 particles). Each ladder operator has a single non-zero entry of value 1. For example, the operator that transitions from the lowest to the second-lowest energy eigenstate is:

$$E_{0\to1} = \begin{pmatrix} 0 & 0 & \dots & 0 \\ 1 & 0 & 0 & \dots \\ 0 & 0 & 0 & \dots \\ \vdots & & \dots & \vdots \\ 0 & \dots & 0 & 0 \end{pmatrix}. \tag{4.10}$$

To incorporate these transitions into the Lindblad equation, the energy jump operators $L_{i\to j}$ are defined as:

$$L_{i\to j} = \sqrt{k_{i\to j}} E_{i\to j}, \tag{4.11}$$

where $i \to j$ denotes the transition from energy eigenstate $|i\rangle$ to $|j\rangle$. The transition rate $k_{i\to j}$ is given by:
For $E_i \neq E_j$:

$$k_{i\to j} = \frac{\epsilon_{ij}}{e^{\epsilon_{ij}/k_B T} - 1} J_{\text{surf}}^2 \sum_{\sigma_k,\sigma_k'} \sum_{n=1}^{N} |\langle i\sigma_k | \sigma \cdot S(n) | j\sigma_k' \rangle|^2, \tag{4.12}$$

and for $E_i = E_j$:

$$k_{i\to j} = k_B T J_{\text{surf}}^2 \sum_{\sigma_k,\sigma_k'} \sum_{n=1}^{N} |\langle i\sigma_k | \sigma \cdot S(n) | j\sigma_k' \rangle|^2. \tag{4.13}$$

Here, the transition rate depends on the Boltzmann factor, the temperature $T$, and the energy difference $\epsilon_{ij}$ between the eigenstates. The sum covers all possible spin states of the scattering electron ($\sigma_k$ and $\sigma'_k$), so we sum over products of the Pauli matrices with the spin operators in the $\hat{x}$, $\hat{y}$, and $\hat{z}$ directions in the term $\hat{\sigma} \cdot \hat{S}$. The joint state projections of the eigenstates $|i\rangle$ and $|j\rangle$ with the electron spin states are computed. The coupling strength between the atoms and the substrate is represented by $J_{\text{surf}}$. Importantly, while $k_{i \to j}$ describes the transitions between energy eigenstates, the states involved in the summation are calculated on the spin basis. However, it should be noted that pure dephasing is not captured in this form of the Lindblad operators, as the jump operators only account for energy transitions (relaxations and excitations). Capturing pure dephasing would require a diagonal term with a negative sign, similar to the $S_z$ operator, which is not present here.

# Chapter 5

# Results

This chapter explores the properties of spin structures on an MgO lattice, where we focus on a square, triangular, and a hexagonal configuration. The analysis is divided into three key sections, each addressing a fundamental aspect of the system's behaviour. All results are based on analytical calculations and numerical simulations, with no experimental data involved.

First, we examine the dominant contributions to the Hamiltonian: exchange and dipolar couplings in Section 5.1. Their relative strengths depend on interatomic distance and spin geometry, determining the system's overall behaviour. By varying these parameters, we identify the transition between exchange- and dipolar-dominated regimes.

Next, Section 5.2 analyses the eigenvalues and eigenstates of the system Hamiltonian. The energy spectrum highlights differences between strong exchange and strong dipolar coupling regimes, showing how the eigenstates and energies evolve with distance and applied magnetic field strength.

Finally, we study the time evolution of the spin structures after spin-flipping under different interatomic distances, magnetic field strengths, and initial spin configurations in Section 5.3. By examining individual spins and spin pairs, we identify decoherence mechanisms and oscillation patterns. In particular, we explore the effects of flipping an outer or central spin in the hexagonal structure, highlighting the role of symmetry and interaction strength.

## 5.1 Exchange and Dipole-Dipole Coupling Decay

In this section, we plot the exchange and dipolar coupling for a $2 \times 2$ square and a hexagonal configuration as a function of interatomic distance. This serves multiple purposes: first, to identify the distances where exchange coupling dominates and where dipolar coupling takes over; second, to examine how deviations from an ideal hexagonal structure, due to the underlying square lattice, affect the coupling strengths.

From Section 3.1.2 we have the following relation for the coupling parameter $J$:

$$J = J_0 \exp\left[\frac{-(r - r_0)}{d_{ex}}\right], \tag{5.1}$$

where $r$ represents the interatomic distance, $r_0 = 8.64\text{Å}$ is the distance of three lattice constants, and $d_{ex} = 0.40 \pm 0.02\text{Å}$ is the characteristic decay length. At $r_0$, $J_0 = 0.97 \pm 0.03$ GHz is the strength of the exchange coupling.

For the dipolar coupling constant we take:

$$D_0 = \frac{\mu_0 \gamma_a \gamma_b \hbar^2}{4\pi r^3} \tag{5.2}$$

Here, $\mu_0$, $\gamma_a$ and $\gamma_b$ are vacuum permeability and gyromagnetics ratio for spin particle $a$ and $b$, respectively, and $r$ is the interatomic distance.

### Square Lattice

The interaction constants as a function of distance are shown in Figure 5.1 for a square system of four spins. The atomic arrangement of this structure is depicted in Figure 3.8. Within the square lattice, six distinct atom pairs are possible, leading to six decay profiles for both exchange and dipolar coupling. However, symmetry reduces these pairings to two categories: vertical/horizontal and diagonal. This symmetry is evident in Figure 5.1, which displays only two distinct decay curves for each coupling constant. Therefore, we can group the decay curves.

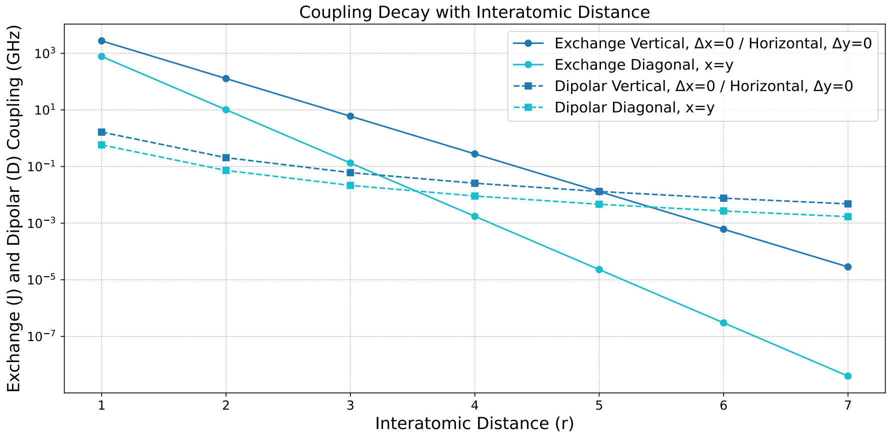

Figure 5.1: Decay curves for exchange and dipolar coupling for all atom pairings in a square system of four spins. Coupling strength is plotted in GHz on the y-axis, over interatomic distance $r$ in lattice constants on the xy-plane.

The logarithmic scale highlights the exponential decay characteristic of the exchange coupling and the $\frac{1}{d^3}$ dependence of the dipolar coupling. Furthermore, the decay of the coupling constants shows three distinct regimes based on distance: for distances up to three lattice constants, exchange coupling dominates; beyond six lattice constants, dipolar coupling becomes predominant; and in the intermediate range of four to five lattice constants, both interactions contribute comparably.

## Hexagonal Lattice

For a hexagonal 7-spin Ti lattice, the interaction constants as a function of distance are shown in Figure 5.2. The atomic configuration of this structure is depicted in Figure 3.10. The grouped decay curves are presented in Figure 5.2. Again, we can divide the region into three, similar to the square lattice: at an interatomic distance of two lattice constants, exchange coupling dominates; beyond six lattice constants, dipolar coupling dominates; and in the intermediate region of four to five lattice constants, they both contribute comparably. In a hexagon of symmetric angles and edges, symmetry reduces the grouped decay curves to six distinct curves

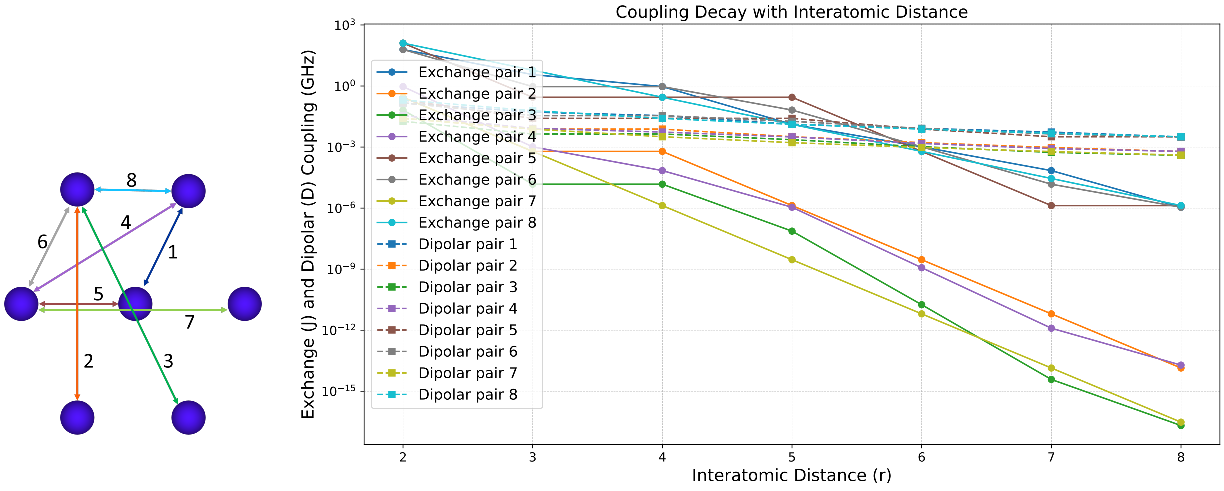

(a) (b)

Figure 5.2: (a) Diagram of possible spin pairs in a hexagonal structure of seven spins. (b) Decay curves for exchange and dipolar coupling in a 7-atom hexagon, grouped over possible spin pairs. Coupling strength is plotted in GHz on the y-axis, over interatomic distance $r$ in lattice constants on the x-axis.

because all atoms pairs can be divided over six interatomic distances. However, the imperfection introduced by the hexagonal arrangement on the square lattice results in eight distinct curves (Figure 5.2a). Still, these eight curves can be categorised into the six groups that correspond to a perfect hexagon, by combining pairs 1 and 6, and 5 and 8. To delve into the effects of the hexagonal imperfections, we take a closer look at the decay curves for a range of distances and the hexagonal configuration at these distances.

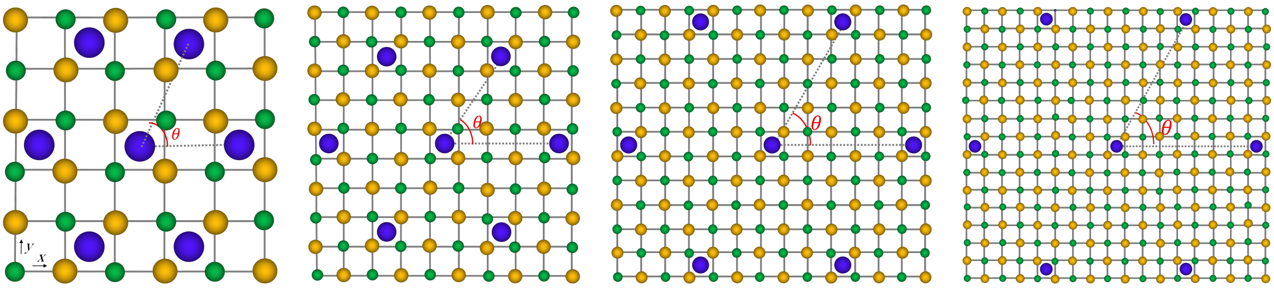

(a) r=2 (b) r=4 (c) r=6 (d) r=8

Figure 5.3: Approximate hexagonal configuration on a square lattice, showing the interaction angles at horizontal distances $r = 2, 4, 6, 8$. The distances between the atoms at angles $\theta$ are shown in Table 5.1.

The hexagons at distances $r = 2, 4, 6, 8$ are plotted in Figure 5.3. Here, distance $r$ refers to the interatomic distance along the x-axis, and the hexagons are configured according to distance $r$ and $\theta = 60°$, where the atoms above and below the midline are placed a the nearest site to $(\pm d \cos\theta, \pm \sin\theta)$. Table 5.1 summarises the effect of distance on the hexagonal configuration. The table provides the angle to the midline for distances ranging from 2 to 8 lattice constants, as well as the composition of the placement sites $(b)$ and $(c)$, illustrated in Figure 3.7. These sites are classified as mixed or entirely equal.

| **Distance** lattice constants | **Distance at angle $\theta$** lattice constants | **Angle $\theta$ to midline** degrees | **Placement sites** |
|---|---|---|---|
| 2 | 2.23 | 63.43° | Mixed |
| 3 | 3.60 | 56.31° | Mixed |
| 4 | 3.60 | 56.31° | Mixed |
| 5 | 4.47 | 63.43° | Mixed |
| 6 | 5.83 | 59.04° | Equal |
| 7 | 7.21 | 56.31° | Mixed |
| 8 | 8.06 | 60.26° | Mixed |

Table 5.1: Hexagonal configuration for distances $r = 2, 3, \ldots, 7, 8$ determined by the angle $\theta$ to the midline, the interatomic distance at $\theta$, and the composition of placement sites as defined in Figure 3.3a. "Mixed" indicates a combination of placement sites (b) and (c), while "Equal" refers to a single placement site among the two.

In Figure 5.2, the decay curves are closely grouped at distances $[6, 8]$. In Table 5.1, the distances $[6, 8]$ more often have an equal placement site configuration and their angles are closer to 60°. Therefore, the variations in lattice configuration have structural impact on the exchange and dipolar coupling constants, and consequently on the system's Hamiltonian.

## 5.2 Eigenvalues

From the coupling constants, we now move on to the eigenvalues of the respective Hamiltonian. Here we focus on two interesting phenomena: twofold degeneracy in odd numbered $\frac{1}{2}$-integer spin systems, called Kramer's degeneracy, and gaps in eigenvalue distributions for small interatomic distances. First, we consider the square lattice of four spins, followed by the triangular lattice of three spins. The triangular lattice serves as a simplified base for the final structure: the hexagonal lattice.

### 5.2.1 Square Lattice

We examine a square lattice of four spins. The analysis consists of two parts: first, we investigate the eigenenergies of the system at different interatomic distances in the absence of an applied magnetic field. Then, we study the effect of four different magnetic field strengths at a fixed interatomic distance $r = 2$ lattice constants.

#### Eigenenergies per Distance

Figure 5.4 presents the eigenenergies for four different interatomic distances, starting at $r = 2$ in the exchange coupling-dominated regime and extending to $r = 5$ in the dipolar coupling-dominated regime. Increasing the interatomic distance causes the initially clustered eigenenergies to gradually spread out. Additionally, the highest and lowest eigenvalues begin to separate from the rest. The highest eigenenergy corresponds to a superposition of the fully aligned up- and down-state, while the lowest eigenenergy corresponds to the singlet state.

There are three degenerate pairs: the first pair consists of the two central eigenenergies, which remain unchanged across all distances. These correspond to the following superpositions:

$$\begin{aligned} |\psi_1\rangle &= \alpha\,|{\downarrow\downarrow\uparrow\uparrow}\rangle + \beta\,|{\uparrow\uparrow\downarrow\downarrow}\rangle\,, \\ |\psi_2\rangle &= \gamma\,|{\downarrow\uparrow\downarrow\uparrow}\rangle + \delta\,|{\uparrow\downarrow\uparrow\downarrow}\rangle\,, \end{aligned} \tag{5.3}$$

with real-valued $\alpha$ and $\beta$, and complex-valued $\gamma$ and $\delta$, which undergo a phase shift as the interatomic distance increases. Notably, at $r = 4$, these states become superpositions of each other, still retaining their real or complex nature.

The remaining two degenerate pairs exhibit time symmetry, but with a phase shift. These two pairs correspond to the triplet state. Within each degenerate pair, one state is a superposition of $S = -1$ spins, while its time-reversed counterpart is a superposition of $S = +1$ spins. This relation holds for $r = 2, 3$, but at $r = 5$, the degenerate eigenstates instead become superpositions of both $S = \pm 1$ spin states, with an intermediate phase transition occurring at $r = 4$.

#### Eigenenergies per Magnetic Field Strength

Figure 5.5 presents the eigenenergies of the same square lattice structure at an interatomic distance of $r = 2$ lattice constants, where the discrete clustering of eigenvalues is most prominent, for four different magnetic field strengths, ranging from weak to strong relative to the coupling strengths in the system. The magnetic field is applied in the positive z-direction, perpendicular to the square structure.

In this system, where an applied magnetic field is present, only the superpositions in equation (5.3) remain degenerate out of the three initially degenerate pairs. The previously degenerate eigenstate pairs are still present, but as the magnetic field increases, their eigenvalues separate proportionally. For example, in Figure 5.5b, the eigenstates corresponding to eigenenergies $E = 133.11$ GHz and $E = -123.02$ GHz are each other's time-reversed state but are no longer degenerate.

Moreover, as the magnetic field strength increases, the eigenvalues reorganise, approaching the expected binomial distribution:

$$\binom{4}{0}, \binom{4}{1}, \binom{4}{2}, \binom{4}{3}, \binom{4}{4}. \tag{5.4}$$

This distribution persists for any $2.5 \cdot 10^3 \leq B \leq 10^{10}$ GHz and presumably for even stronger fields, again representing the possible spin pairings within the system.

The corresponding eigenstates, from high to low eigenenergies, are as follows: the highest for the fully aligned up-state, followed by four superpositions of the triplet $S = 1$ state, six superpositions of the singlet $S = 0$ state, four superpositions of the triplet $S = -1$ state, and finally, the lowest for the fully aligned down-state.

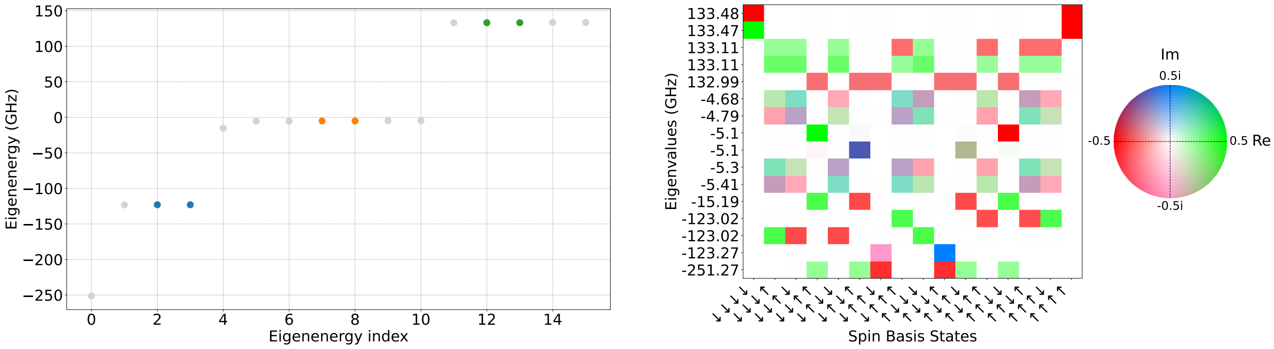

(a) Eigenenergies at $r = 2$

(b) Spin Contributions at $r = 2$

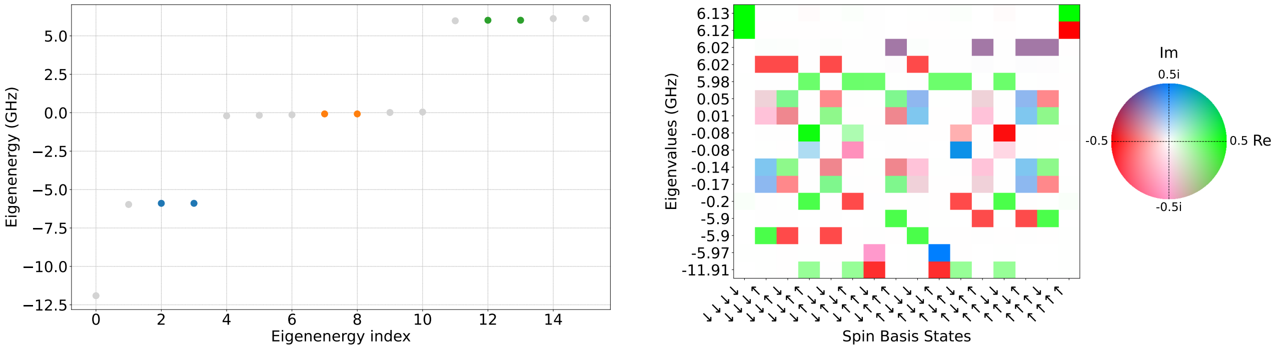

(c) Eigenenergies at $r = 3$

(d) Spin Contributions at $r = 3$

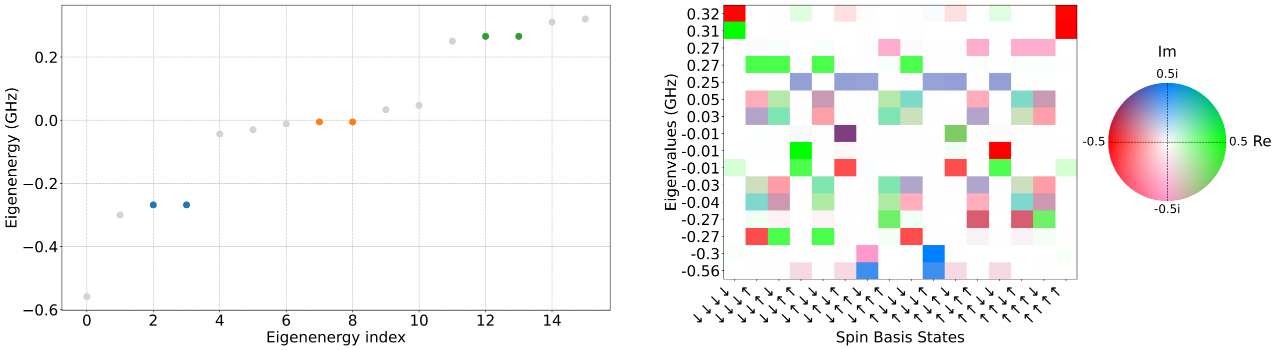

(e) Eigenenergies at $r = 4$

(f) Spin Contributions at $r = 4$

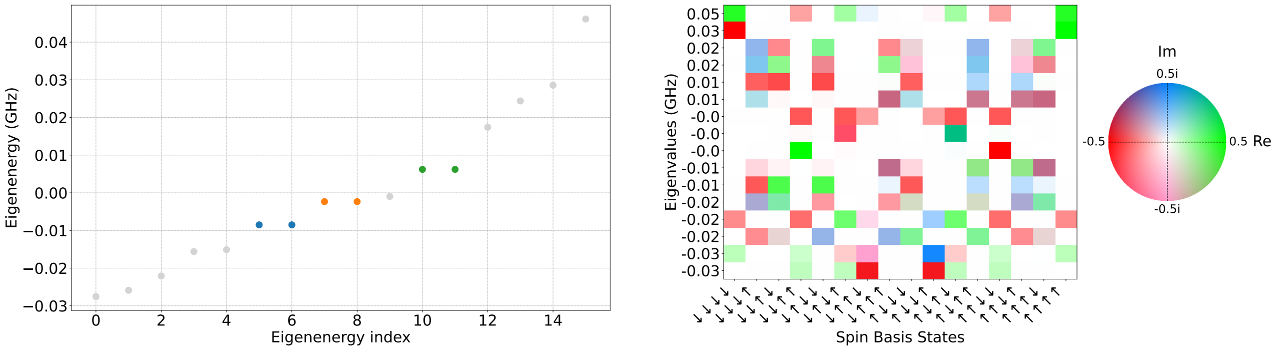

(g) Eigenenergies at $r = 5$

(h) Spin Contributions at $r = 5$

Figure 5.4: Eigenenergies (GHz) for a square lattice of four spins on the xy-plane without an applied magnetic field for distances $r = 2, 3, 4, 5$ lattice constants. The eigenvalues are colour-coded based on their degeneracy, with eigenvalues considered degenerate if their values fall within a relative tolerance of $10^{-12}$. (b) Complex heatmap representation of the contributions of spin basis states at these eigenenergies. The heatmap is scaled from 0 (white) to 0.5 (green, blue, red, pink for $1, i, -1, -i$ respectively), indicating the contribution intensity.

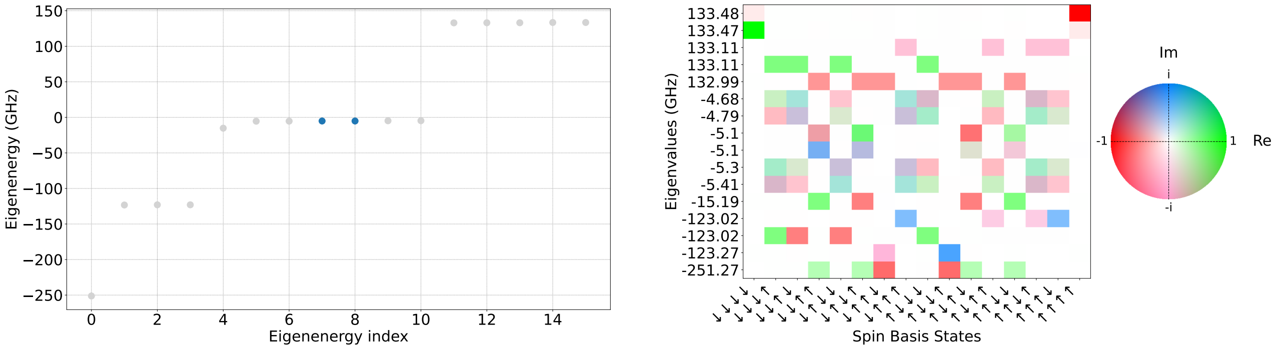

(a) Eigenenergies at $B = 2.5 \cdot 10^{-3}$ GHz

(b) Spin Contributions at $B = 2.5 \cdot 10^{-3}$ GHz

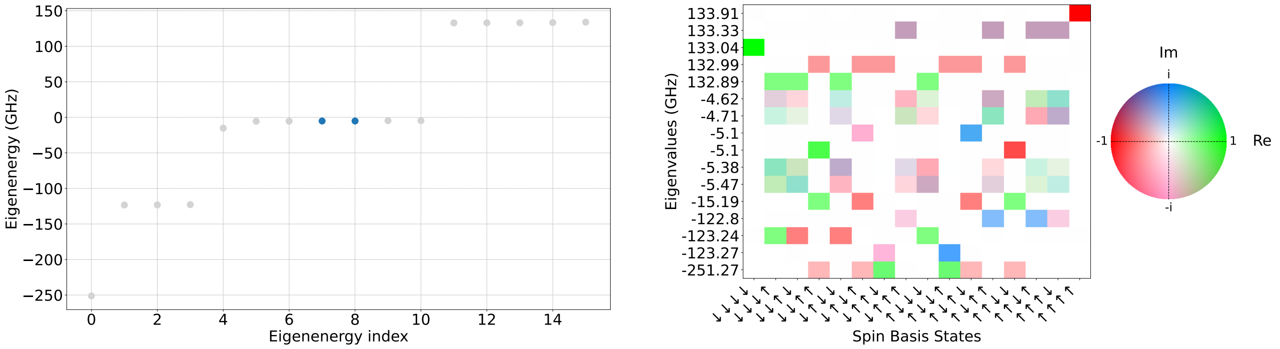

(c) Eigenenergies at $B = 2.5 \cdot 10^{-1}$ GHz

(d) Spin Contributions at $B = 2.5 \cdot 10^{-1}$ GHz

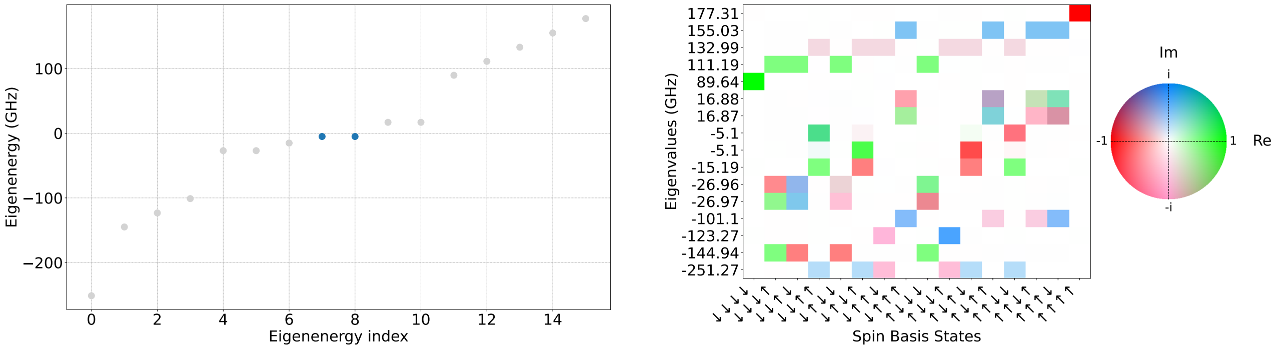

(e) Eigenenergies at $B = 2.5 \cdot 10^{1}$ GHz

(f) Spin Contributions at $B = 2.5 \cdot 10^{1}$ GHz

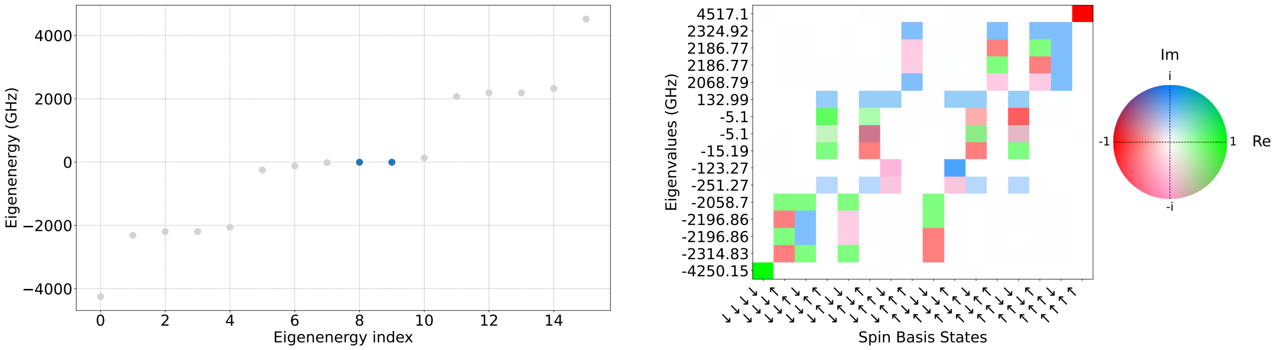

(g) Eigenenergies at $B = 2.5 \cdot 10^{3}$ GHz

(h) Spin Contributions at $B = 2.5 \cdot 10^{3}$ GHz

Figure 5.5: Eigenenergies (GHz) for a square lattice of four spins on the xy-plane, configured at $r = 2$ lattice constants. The eigenvalues are colour-coded based on their degeneracy, with eigenvalues considered degenerate if their values fall within a relative tolerance of $10^{-12}$. The system is shown for four different applied magnetic field strengths perpendicular to the xy-plane, increasing from top to bottom, followed by a complex heatmap representation of the contributions of spin basis states at the eigenenergies. The heatmap is scaled from 0 (white) to 1 (green, blue, red, pink for $1, i, -1, -i$ respectively), indicating the contribution intensity.

The degeneracy found in for the square lattice of four spins does not imply a systemic rule for even numbered system. For a system of six spins for example, there are no degenerate pairs, regardless of the magnetic field strength.

### 5.2.2 Triangular Lattice

Due to the size of the hexagonal system, we will visualise the degeneracy in eigenvalues and time-symmetric eigenstates of a smaller odd-numbered system: a triangle of three spins. Figure 5.6 shows the eigenenergies of the system at interatomic distances of $r = 2, 4, 6, 8$ lattice constants, followed by the contributions of the spin states for each eigenstate corresponding to the respective eigenenergy.

**Kramer Degeneracy**

At each distance, the eigenvalues are two-fold degenerate within the specified relative tolerance up to 12 decimals. Kramer's theorem explains this effect, which is caused by time-reversal symmetry in the system because there is no applied magnetic field. More specifically, the time-reversal operation in a Hilbert space $\mathcal{H}$ is defined as an antiunitary operator $\mathcal{T} : \mathcal{H} \to \mathcal{H}$. If the relation $\mathcal{T}^2 = (-1)^{2S} = -1$ holds, where $S$ is the total spin number of the system, then Kramer's theorem states that for any vector $v$ in $\mathcal{H}$, its time-reversed counterpart $\mathcal{T}v$ is orthogonal to $v$. Since the system's Hamiltonian commutes with the time-reversal operator, the spin state $v$ and its time-reversed state $\mathcal{T}v$ must share the same energy. This results in the observed degeneracy in a system consisting of an odd number of half-integer spin particles and no applied magnetic field [28].

**Eigenenergies per Distance**

Similar to the square lattice, the initially clustered eigenenergies gradually spread out for increasing interatomic distance. Because there are only four pairs of eigenvalues, the highest and lowest eigenvalues are already separated from the rest. The eigenstates corresponding to the highest eigenvalues are again the fully aligned up- and down-state. For increasing distance they develop to be superpositions of the fully aligned up-state combined with the doublet state of $S = -\frac{1}{2}$, and down-state combined with the doublet state of $S = +\frac{1}{2}$. The eigenstates corresponding to the lowest eigenvalues at $r = 2$ are:

$$|\psi_1\rangle = \alpha\,|{\downarrow\uparrow\downarrow}\rangle + \beta\,|{\uparrow\downarrow\downarrow}\rangle \tag{5.5}$$

and,

$$|\psi_2\rangle = \gamma\,|{\downarrow\uparrow\uparrow}\rangle + \delta\,|{\uparrow\downarrow\uparrow}\rangle\,. \tag{5.6}$$

These are two superpositions of states with $S = -\frac{1}{2}$ and $S = +\frac{1}{2}$ respectively. At increasing distance $r = 4$ these eigenstates are still present, but no longer represent the lowest eigenenergies: they are replaced by the doublet states. The doublet states are eigenstates of the system for all distances, and sometimes even for four eigenvalues, where they are distinguishable by phase factors. At distances $r = 4, 5$, the lowest eigenvalues are superposition of the doublet state and the fully aligned up- and down-state, like the highest eigenvalues differing by phase factors.

**Eigenenergies per Magnetic Field Strength**

Figure 5.7 presents the eigenenergies of the triangle structure of three spins at an interatomic distance of $r = 2$ lattice constants, where the discrete clustering of eigenvalues is most prominent, for four different magnetic field strengths, ranging from weak to strong relative to the coupling strengths in the system. The magnetic field is applied in the positive z-direction, perpendicular to the square structure.

Due to the applied magnetic field, none of the previously degenerate pairs remains. The time-reversed pairs are still visible, but slight differences in the spin contributions to the eigenstate introduce splitting in the eigenvalues proportional to the magnetic field strength and remove the degeneracy.

Similarly to the square lattice the magnetic field reorganises the eigenvalues from separated pairs to a uniform distribution and finally a binomial distribution. These changes are accompanied by little change in the spin contributions to the eigenstates. There the increasing magnetic field in the positive z-direction lowers the eigenenergy corresponding to the down-state, but next to that the eigenstates are roughly the same up to phase factor. The corresponding resulting eigenstates in the binomial distribution, from high to low eigenenergies, are as follows: the highest for the fully aligned up-state, followed by three superpositions of the triplet $S = +\frac{1}{2}$ state, three superpositions of the triplet $S = -\frac{1}{2}$ state, and finally, the lowest for the fully aligned down-state.

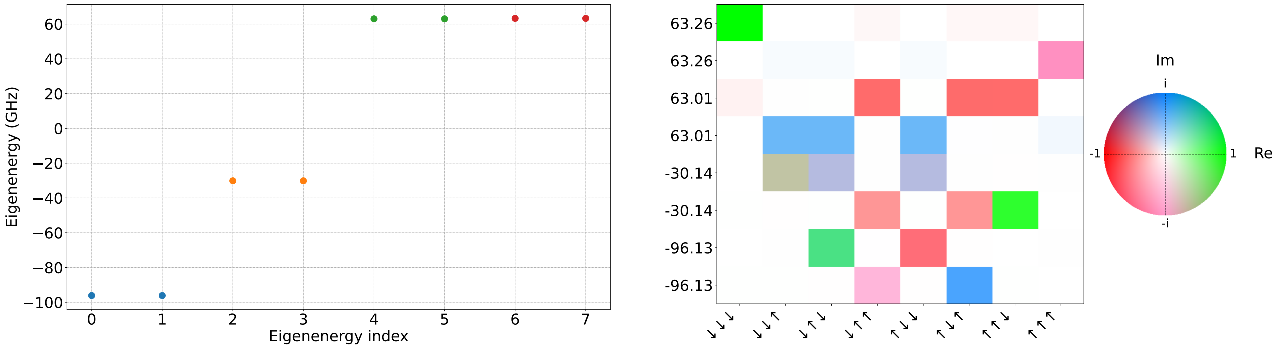

(a) Eigenenergies at $r = 2$ (b) Spin Contributions at $r = 2$

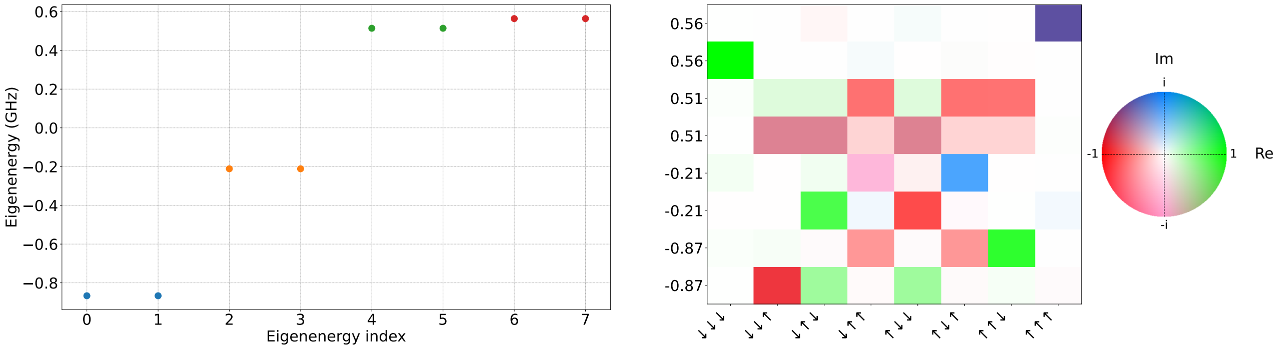

(c) Eigenenergies at $r = 4$ (d) Spin Contributions at $r = 4$

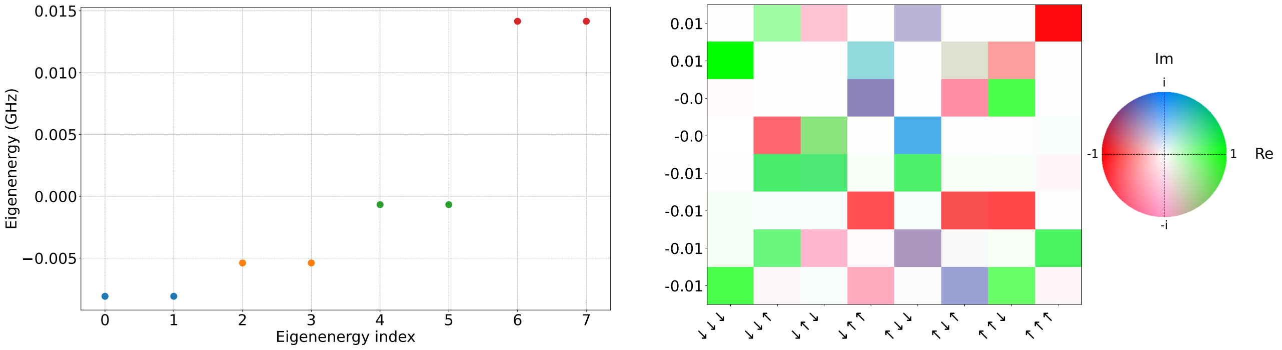

(e) Eigenenergies at $r = 6$ (f) Spin Contributions at $r = 6$

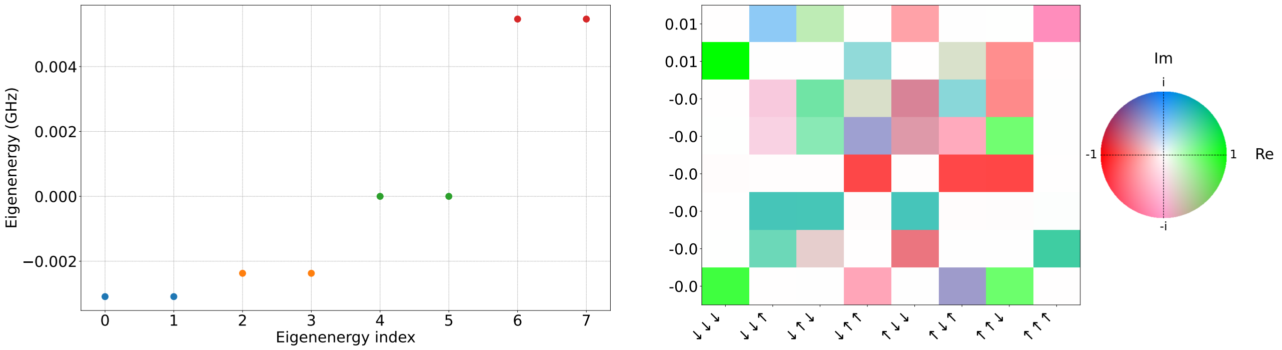

(g) Eigenenergies at $r = 8$ (h) Spin Contributions at $r = 8$

Figure 5.6: Eigenenergies (GHz) for a triangular lattice of three spins on the xy-plane without an applied magnetic field for distances $r = 2, 4, 6, 8$ lattice constants. The eigenvalues are colour-coded based on their degeneracy, with eigenvalues considered degenerate if their values fall within a relative tolerance of $10^{-12}$. (b) Complex heatmap representation of the contributions of spin basis states at these eigenenergies. The heatmap is scaled from 0 (white) to 0.5 (green, blue, red, pink for $1, i, -1, -i$ respectively), indicating the contribution intensity.

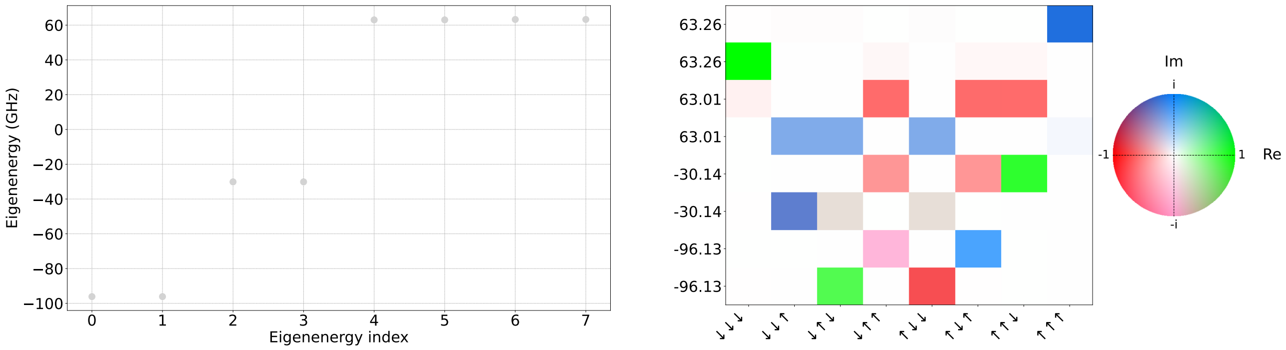

(a) Eigenenergies at $B = 2.5 \cdot 10^{-3}$ GHz (b) Spin Contributions at $B = 2.5 \cdot 10^{-3}$ GHz

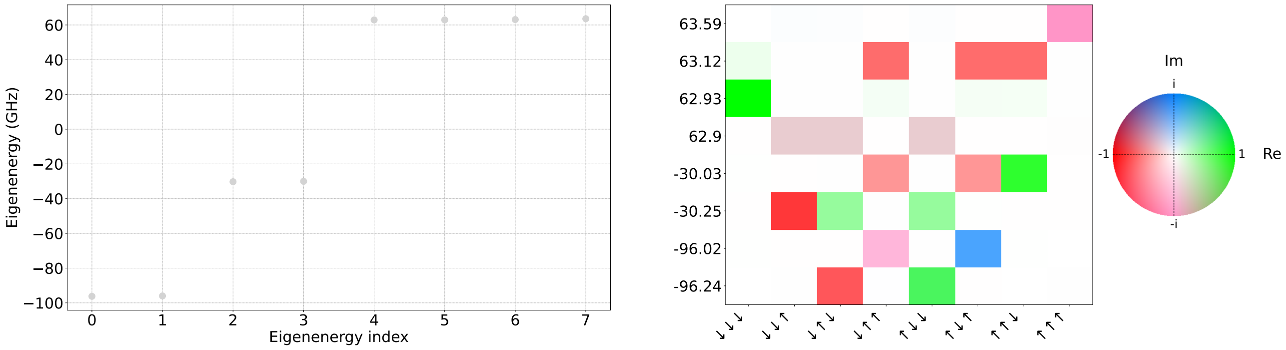

(c) Eigenenergies at $B = 2.5 \cdot 10^{-1}$ GHz (d) Spin Contributions at $B = 2.5 \cdot 10^{-1}$ GHz

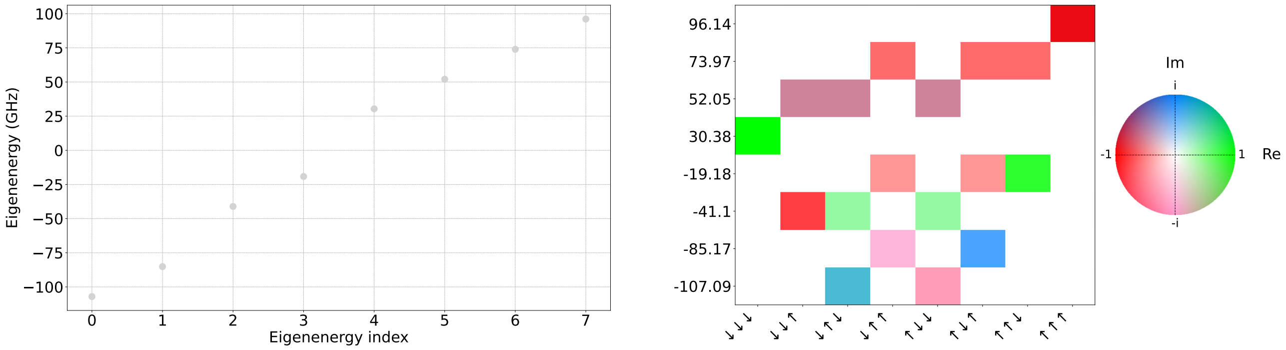

(e) Eigenenergies at $B = 2.5 \cdot 10^{1}$ GHz (f) Spin Contributions at $B = 2.5 \cdot 10^{1}$ GHz

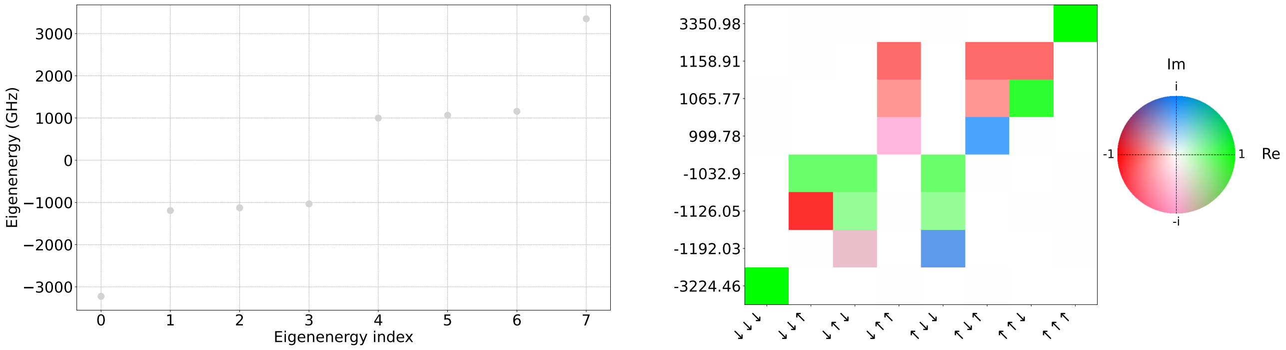

(g) Eigenenergies at $B = 2.5 \cdot 10^{3}$ GHz (h) Spin Contributions at $B = 2.5 \cdot 10^{3}$ GHz

Figure 5.7: Eigenenergies (GHz) for a triangular lattice of three spins on the xy-plane, configured at $r = 2$ lattice constants. The eigenvalues are colour-coded based on their degeneracy, with eigenvalues considered degenerate if their values fall within a relative tolerance of $10^{-12}$. The system is shown for four different applied magnetic field strengths perpendicular to the xy-plane, increasing from top to bottom, followed by a complex heatmap representation of the contributions of spin basis states at the eigenenergies. The heatmap is scaled from 0 (white) to 1 (green, blue, red, pink for $1, i, -1, -i$ respectively), indicating the contribution intensity..

### 5.2.3 Hexagonal Lattice

Next, we consider the hexagonal lattice. The decay in exchange and dipolar coupling shows a region of interest between distances of $r = 2$ lattice constants, where the exchange coupling dominates, and $r = 8$, where the dipolar coupling becomes dominant. Between these two points lies an intermediate region where the coupling strengths are approximately equal. To explore the impact of these couplings on the structure's Hamiltonian, we analyse the eigenenergies in the intermediate region without the corresponding eigenstates due to the size of the system. The eigenenergies of the Hamiltonian for distances $[2, 4, 6, 8]$ without an applied magnetic field are shown in Figure 5.8.

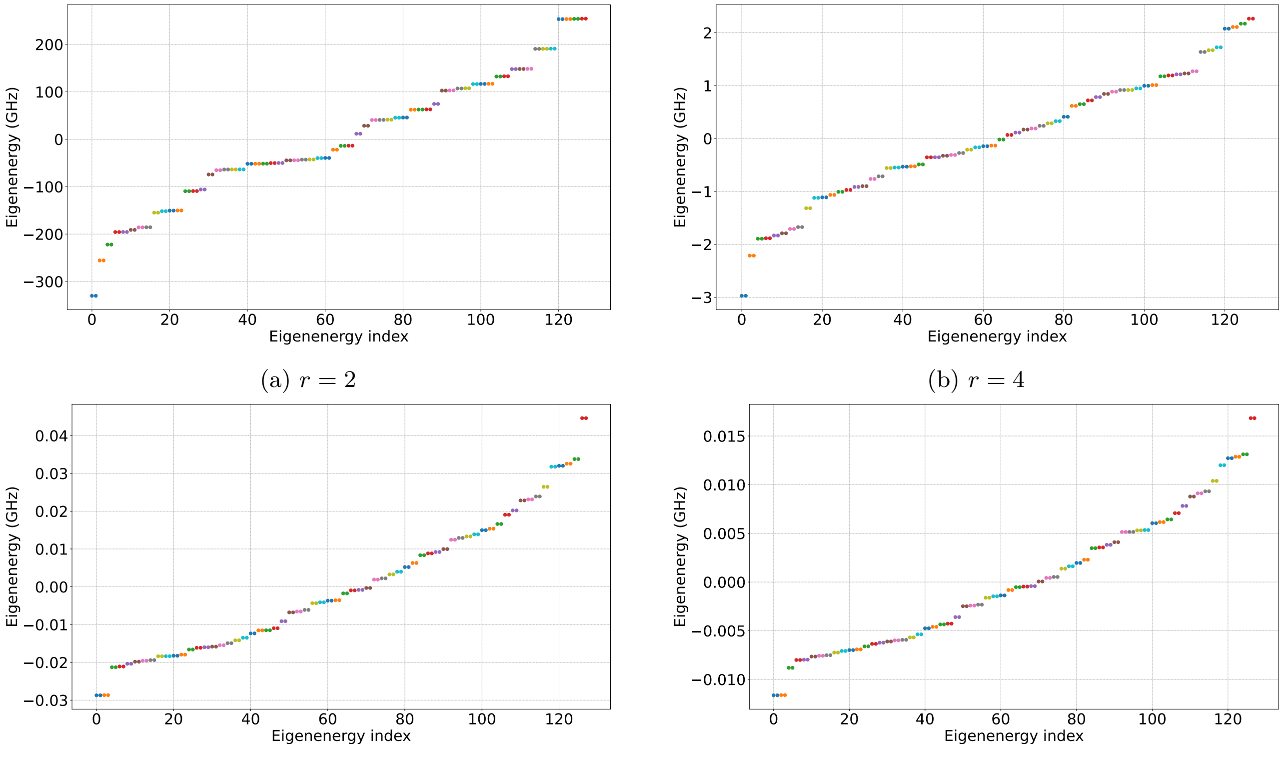

(a) $r = 2$

(b) $r = 4$

(c) $r = 6$

(d) $r = 8$

Figure 5.8: Eigenenergies in GHz of a 7-atom hexagon for four interatomic distances, expressed in lattice constants, without an applied magnetic field. The eigenvalues are colour-coded based on their degeneracy, with eigenvalues considered degenerate if their values fall within a relative tolerance of $10^{-12}$.

#### Eigenenergy Distribution

Considering the previous results for both the hexagon (Figure 5.8) and the triangle (Figure 5.6), we observe stepwise clustering of the eigenenergies around the middle eigenenergy at distance $r = 2$. These clusters spread out for increasing distance, where the top and bottom Kramers pairs separate from the rest.

The top Kramers pair consists of the fully spin-up and spin-down states at $r = 2$. However, this is no longer the case for $r = 8$, where the top pair of states become superpositions, although still predominantly aligned with the up and down states. Meanwhile, the bottom eigenstates form superpositions of multiple spin states. The largest contributions to these superpositions come from 31 spin basis states, each corresponding to either $S = +\frac{1}{2}$ or $S = -\frac{1}{2}$.

The eigenstate corresponding to $S = +\frac{1}{2}$ is nearly identical to the doublet state, except for missing contributions from the following spin basis states:

$$|{\uparrow\downarrow\downarrow\downarrow\uparrow\uparrow\uparrow}\rangle\,, \quad |{\uparrow\uparrow\downarrow\downarrow\downarrow\uparrow\uparrow}\rangle\,, \quad |{\downarrow\uparrow\uparrow\uparrow\downarrow\downarrow\uparrow}\rangle\,, \quad |{\downarrow\downarrow\uparrow\uparrow\uparrow\downarrow\uparrow}\rangle\,. \tag{5.7}$$

For a system of seven spins arranged in a one-dimensional chain, the eigenstates corresponding to the lowest eigenenergies form doublet states. However, in the hexagonal structure, asymmetry and the presence of a central spin prohibit the spin states listed in equation (5.7).

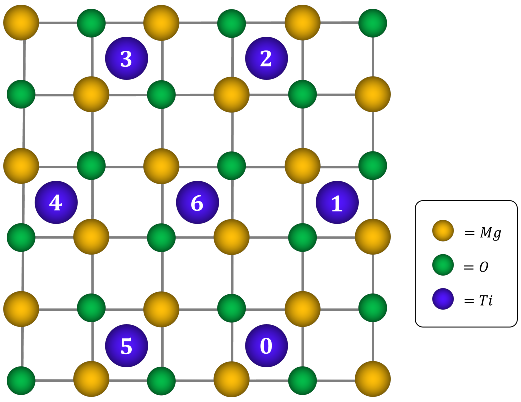

Figure 5.9: Hexagonal spin structure on a square MgO lattice, including spin numbering.

To understand this restriction, we consider the numbering of the spins, illustrated in Figure 5.9. For $S = +\frac{1}{2}$, the missing spin states all share the characteristic that atom $n = 6$ is spin-up, while the outer ring of the hexagon is symmetrically divided into three spin-up and three spin-down atoms. Due to the asymmetry introduced by the square MgO lattice, the only symmetric way to partition the outer hexagonal ring is into two groups: $\{0, 1, 2\}$ and $\{3, 4, 5\}$. The missing spin states, however, exhibit an asymmetric division into $\{4, 5, 0\}$ and $\{1, 2, 3\}$ or $\{5, 0, 1\}$ and $\{2, 3, 4\}$, which is not permitted in this system.
A similar observation holds for the eigenstate corresponding to $S = -\frac{1}{2}$, which matches the doublet state except for missing contributions from the following spin basis states:

$$|{\downarrow\uparrow\uparrow\uparrow\downarrow\downarrow\downarrow}\rangle\,, \quad |{\downarrow\downarrow\uparrow\uparrow\uparrow\downarrow\uparrow}\rangle\,, \quad |{\uparrow\downarrow\downarrow\uparrow\uparrow\downarrow\downarrow}\rangle\,, \quad |{\uparrow\uparrow\downarrow\uparrow\downarrow\downarrow\downarrow}\rangle\,. \tag{5.8}$$

Unlike the case for $S = +\frac{1}{2}$, no clear structural pattern emerges in the missing spin states for $S = -\frac{1}{2}$.

### Magnetic Field Dependence of Eigenenergies

Next, we examine the eigenvalues at the intermediate distance $r = 5$ for the hexagonal lattice and analyse the system under various nonzero magnetic fields applied perpendicular to the plane. Figure 5.10 presents the eigenenergies for four different field strengths, ranging from weak to strong relative to the coupling strengths.
For magnetic fields weaker than $2.5 \cdot 10^{-3}$ GHz, the eigenenergies exhibit an asymmetric distribution (Figure 5.10a), with 72 positive eigenvalues and 56 negative eigenvalues. Negative eigenvalues are spaced in discrete steps, while positive eigenvalues form a nearly smooth curve. As the magnetic field strength increases (Figures 5.10b and 5.10c), the system approaches a more symmetric energy distribution. For fields stronger than 2.5 GHz, the eigenenergies become evenly distributed, aligning symmetrically at the positive and negative ends of the spectrum (Figure 5.10d).

### Eigenvalue Distribution and Binomial Coefficients

The eigenvalue distribution follows binomial coefficients, which, for a hexagonal structure consisting of seven spins, are given by:

$$\binom{7}{0} = 1, \binom{7}{1} = 7, \binom{7}{2} = 21, \binom{7}{3} = 35, \binom{7}{4} = 35, \binom{7}{5} = 21, \binom{7}{6} = 7, \binom{7}{7} = 1. \tag{5.9}$$

These coefficients represent the possible spin pairings within the system.

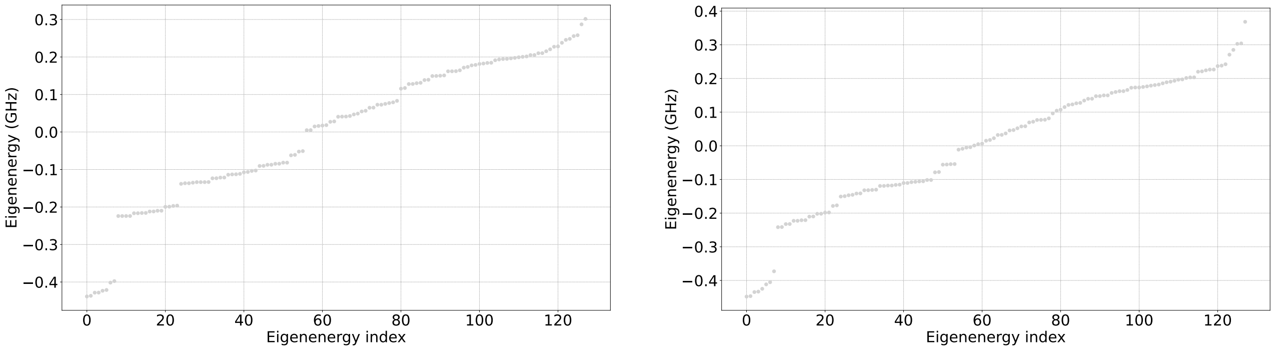

(a) $B = 2.5 \cdot 10^{-3}$ GHz (b) $B = 2.5 \cdot 10^{-2}$ GHz

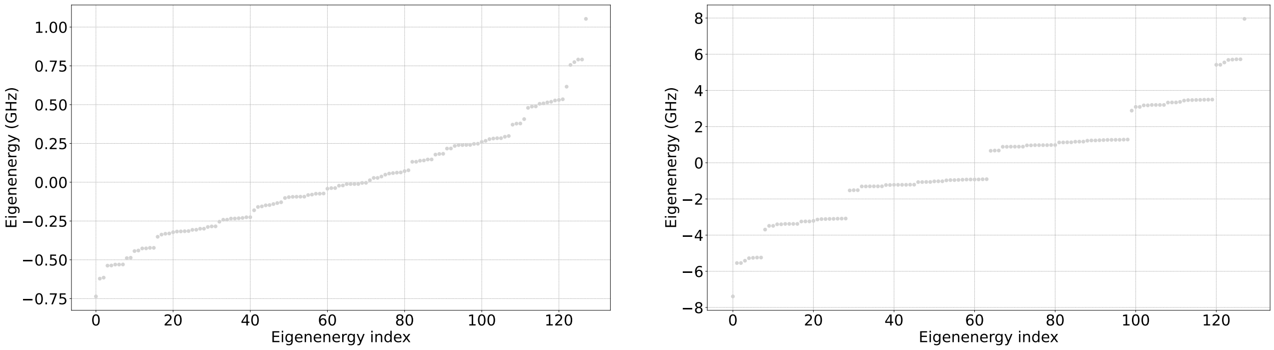

(c) $B = 2.5 \cdot 10^{-1}$ GHz (d) $B = 2.5$ GHz

Figure 5.10: Eigenenergies (GHz) of a seven-atom hexagon at interatomic distances $r = 5$ (expressed in lattice constants), for four different applied magnetic field strengths. There are no degenerate eigenvalues.

## 5.3 Spin Flipping

In this section, we investigate the decoherence of atomic spins within square and hexagonal lattices placed on an MgO surface. Specifically, we analyse the previously discussed regimes of exchange coupling, dipolar coupling, and the intermediate regime. The decoherence rates are determined using the Kondo model described in Section 3.4. For all systems, we apply a uniform surface coupling of $8 \cdot 10^{-3}$ GHz to all spins.

For most systems, the initial state corresponds to the ground state of the Hamiltonian. The ground state depends on system size, interatomic distance, and applied magnetic field, which we vary accordingly. However, the experiment does not utilise the ground state directly but rather the equilibrium state of the system. At the experimental temperature of 0.3 K, corresponding to 6 GHz, the ground state effectively coincides with the equilibrium state for the systems we model. For larger interatomic distances, however, 6 GHz becomes relatively large compared to the system energy scales, and the ground state approximation no longer holds. To maintain accuracy, we consider the equilibrium state in the following analyses instead of the ground state.

The specifics of which spin is flipped are discussed per structure. After applying the spin flip, the density matrix is renormalised, ensuring energy conservation within the system. If energy dissipation were assumed during the spin flip, the qualitative behaviour of the results would remain unchanged but scaled to lower values.

We explore the following structures: a square structure of four spins, a triangle of three spin, and a hexagonal arrangement.

### 5.3.1 Square Lattice

We consider the square structure for distance $r = 3, 4, 5, 6$ lattice constants, ranging from a dominant exchange coupling to a dominant dipolar coupling, discussed in Section 5.1. The applied magnetic field is varied from $2.5 \cdot 10^{1}$ GHz to $2.5 \cdot 10^{-3}$ GHz along the $z$-axis perpendicular to the system. The system is initialised in its equilibrium state, which depends on the interatomic distance, magnetic field strength and temperature. For a strong magnetic field, the equilibrium state is $|\uparrow\uparrow\uparrow\uparrow\rangle$, whereas for zero magnetic field, the equilibrium state corresponds to the singlet state of a four-spin system. For any intermediate magnetic field, the system sill resembles the singlet state but increasingly favours $|\uparrow\uparrow\uparrow\uparrow\rangle$ over $|\downarrow\downarrow\downarrow\downarrow\rangle$ in proportion to the magnetic field strength.

Figure 5.11 shows the time evolution of the square structure, where spin $n = 0$ is flipped for the distances and magnetic field strengths discussed in the previous section. Due to the symmetry of the system, the specific choice of spin to flip is inconsequential. At a distance of $r = 3$ lattice constants, the exchange coupling is approximately $10^{3}$ GHz (Figure 5.1), making the previously used time step of $\Delta t = 0.2$ ns insufficiently small, resulting in aliasing in Figures 5.11a, 5.11b, 5.11c. To address this, the second row of Figure 5.11 presents zoomed-in frames over a 10 ns window, using a refined time step of $\Delta t = 5 \cdot 10^{-3}$ ns.

With increasing distance, the oscillation frequency decreases, especially from $r = 4$ to $r = 5$, which in Figure 5.1 is precisely the region that shows a transition from exchange-dominant to dipolar-dominant coupling constants. Another observation is the symmetry in the system for a strong magnetic field, as seen in the left column of Figure 5.11. This demonstrates a symmetric relation between spins (1) and (2), and an asymmetric relation between spins (0) and (3). The square system of four spins is numbered as follows: (0) top left, (1) top right, (2) bottom left, (3) bottom right. As expected, the flipped spin (0) and its diagonal counterpart (3) exhibit asymmetric oscillations, whereas the flipped spin (0) its neighbouring spins (1) and (2) show symmetric oscillations. This effect is most clearly visible in Figures 5.11j, 5.11m.

For weaker magnetic fields, the symmetry between the diagonal neighbouring spins (1) and (2) disappears as the interatomic distance decreases. A slight shift appears, for example, in Figure 5.11k, and in Figures 5.11e, 5.11h, the oscillations between spins (1) and (2) are asymmetric. For a nearly zero magnetic field in the right column, the asymmetry between spins (1) and (2) is already visible for $r = 5$ in Figure 5.11(l).

Besides the asymmetry within the diagonal spin pairs, we also observe an asymmetry between the oscillations of the couple spin pairs for the smallest interatomic distances and weak magnetic fields. This effect is most clearly visualised in Figures 5.11b,5.11c,5.11f. Additionally, for the weakest magnetic field, it is also noticeable in Figure 5.11i for $r = 4$ lattice constants.

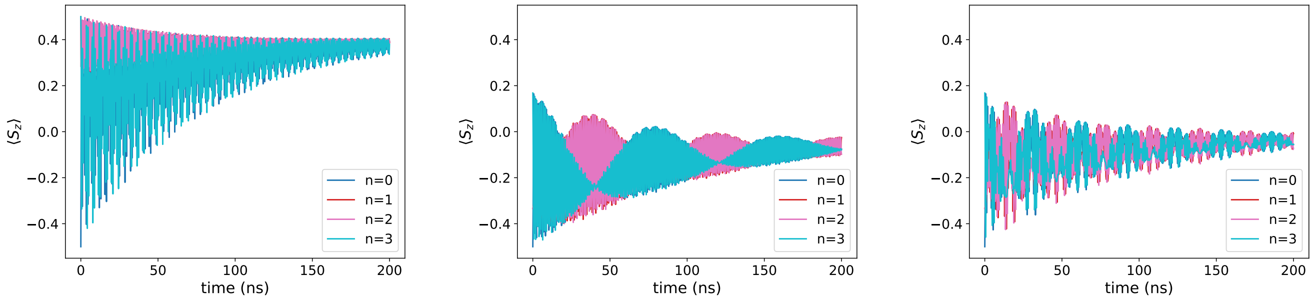

(a) $r = 3$: $2.5 \cdot 10^{1}$ GHz (b) $r = 3$: $2.5 \cdot 10^{-1}$ GHz (c) $r = 3$: $2.5 \cdot 10^{-3}$ GHz

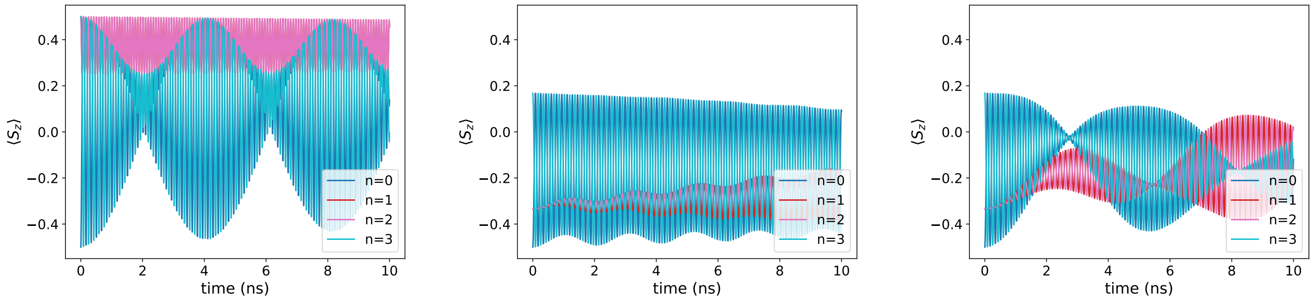

(d) 0-10 ns frame figure (a) (e) 0-10 ns frame figure (b) (f) 0-10 ns frame figure (c)

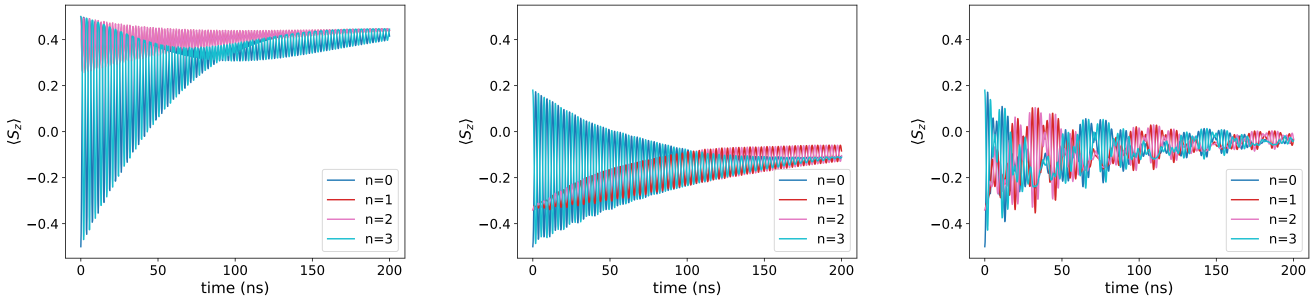

(g) $r = 4$: $2.5 \cdot 10^{1}$ GHz (h) $r = 4$: $2.5 \cdot 10^{-1}$ GHz (i) $r = 4$: $2.5 \cdot 10^{-3}$ GHz

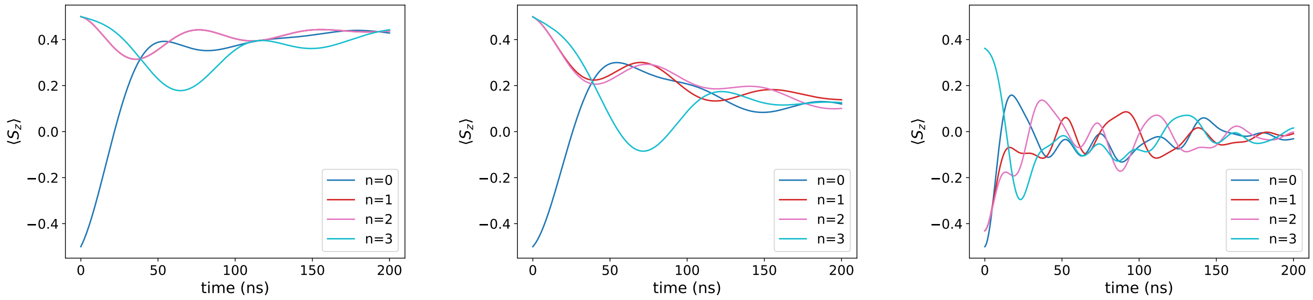

(j) $r = 5$: $2.5 \cdot 10^{1}$ GHz (k) $r = 5$: $2.5 \cdot 10^{-1}$ GHz (l) $r = 5$: $2.5 \cdot 10^{-3}$ GHz

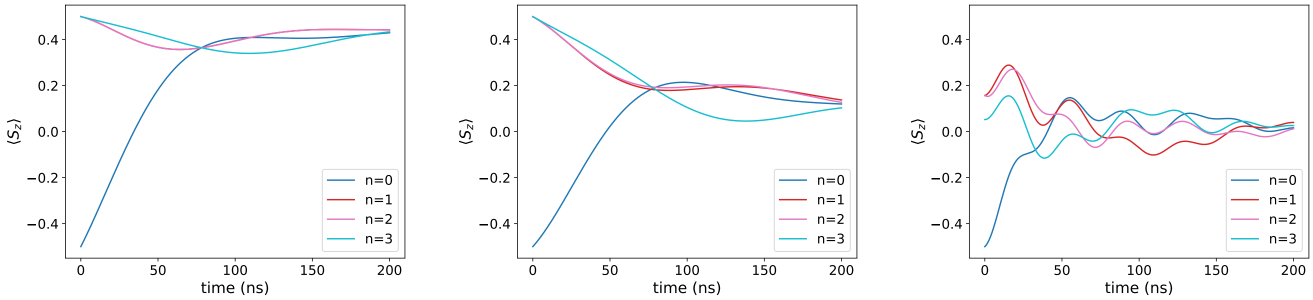

(m) $r = 6$: $2.5 \cdot 10^{1}$ GHz (n) $r = 6$: $2.5 \cdot 10^{-1}$ GHz (o) $r = 6$: $2.5 \cdot 10^{-3}$ GHz

Figure 5.11: Time evolution of the expectation value of the $S_z$ component for a square structure of four spins configured at interatomic distances $r = 3, 4, 5, 6$ lattice constants. The rows represent distances $r = 3, 4, 5, 6$, where the second rows provides a zoomed in frame at 0 to 10 nanoseconds of the first row, while the columns correspond to different applied magnetic fields decreasing from left to right.

### 5.3.2 Triangular Lattice

We examine the triangular spin structure for interatomic distances of $r = 4, 6, 8$ lattice constants, covering the transition from a dominant exchange coupling to a dominant dipolar coupling. A magnetic field is applied along the $z$-axis (perpendicular to the system), varying from $2.5 \cdot 10^1$ GHz to $2.5 \cdot 10^{-3}$ GHz. The system is initialised in its equilibrium state, which depends on both the interatomic distance and the magnetic field strength.
For a strong magnetic field, the equilibrium state is forced into $|\uparrow\uparrow\uparrow\rangle$. In contrast, for zero magnetic field, the equilibrium state forms a superposition of spin states:

$$|\psi\rangle = \alpha\,|\downarrow\downarrow\downarrow\rangle + \beta\,|\downarrow\uparrow\uparrow\rangle + \gamma\,|\uparrow\downarrow\uparrow\rangle + \delta\,|\uparrow\uparrow\downarrow\rangle\,, \tag{5.10}$$

where the coefficients $\alpha, \beta, \gamma, \delta$ depend on the interatomic distances within the triangular structure.
Figure 5.13 presents the time evolution of the system when spin (0) is flipped, considering the distances and magnetic field strengths discussed in the previous section. At $r = 4$ lattice constants, the exchange coupling dominates, making the previously used time step of $\Delta t = 0.2$ ns too large, leading to aliasing effects in Figures 5.13a, 5.13b, 5.13c. To resolve this, the second row of Figure 5.13 provides a zoomed-in view over a window of 10 ns, utilising a refined time step of $\Delta t = 5 \cdot 10^{-3}$ ns.

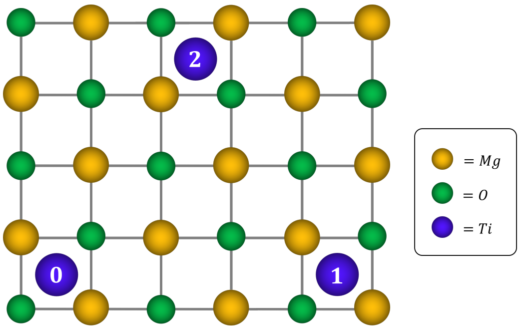

Figure 5.12: Triangular spin structure on a square MgO lattice, including spin numbering.

The numbering of atoms in the triangular structure is depicted in Figure 5.12. At $r = 4$, the triangle's coordinates are $\{(0,0), (4,0), (2,3)\}$, making it symmetric along a vertical axis passing through spin $n = 2$. The system is dominated by exchange coupling, thus we would expect flipping spin (0) should induce oscillations primarily with its nearest neighbour, $n = 2$. As a result, spin $n = 1$ would respond to the combined oscillation of spins 0 and 2. However, due to the asymmetry in distances, where spins 0 and 2 are not equidistant from spin 1, this interaction does not occur as expected due to phase differences. Instead, flipping spin (0) causes an asymmetric response in spin $n = 1$, followed by spin $n = 2$ reacting to the collective oscillations of spins 0 and 1, which are equidistant from it (Figures 5.13d, 5.13e, 5.13f).
For larger distances, the triangular configurations are defined by the coordinates:

- $r = 6$: $\{(0,0), (6,0), (3,5)\}$
- $r = 8$: $\{(0,0), (8,0), (4,7)\}$

In this regime, the applied magnetic field dominates the other interactions, and the small differences in atomic positions no longer significantly impact the oscillation dynamics. Instead, variations manifest primarily in amplitude and phase, as observed in Figures 5.13g, 5.13h. In the rightmost column, where the applied magnetic field no longer dominates, the starting positions of spins 1 and 2 differ are no longer spin-up. Additionally, Figure 5.13i reveals two distinct oscillation frequencies: a slow oscillation between spins 0 and 2, accompanied with fast oscillations for all spins.

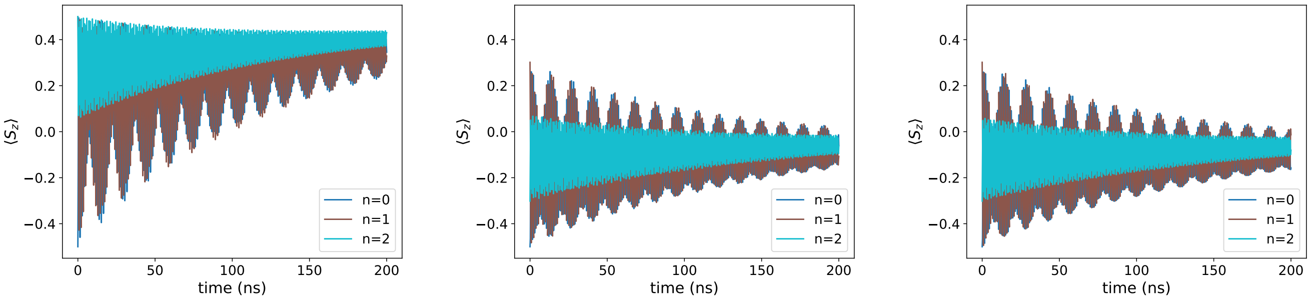

(a) $r = 4{:}\ 2.5 \cdot 10^{1}$ GHz (b) $r = 4{:}\ 2.5 \cdot 10^{-1}$ GHz (c) $r = 4{:}\ 2.5 \cdot 10^{-3}$ GHz

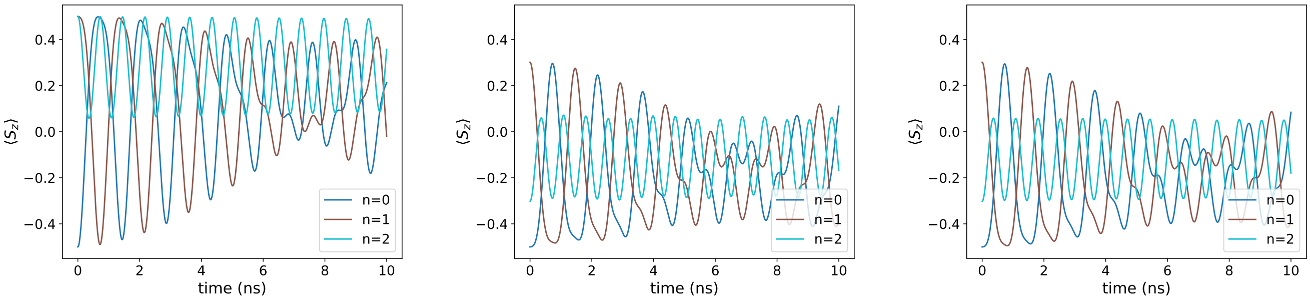

(d) 0-10 ns frame figure (a) (e) 0-10 ns frame figure (b) (f) 0-10 ns frame figure (c)

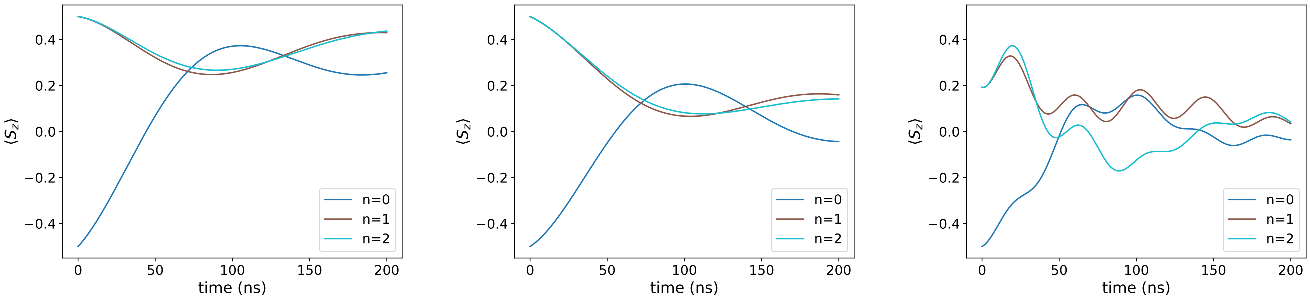

(g) $r = 6{:}\ 2.5 \cdot 10^{1}$ GHz (h) $r = 6{:}\ 2.5 \cdot 10^{-1}$ GHz (i) $r = 6{:}\ 2.5 \cdot 10^{-3}$ GHz

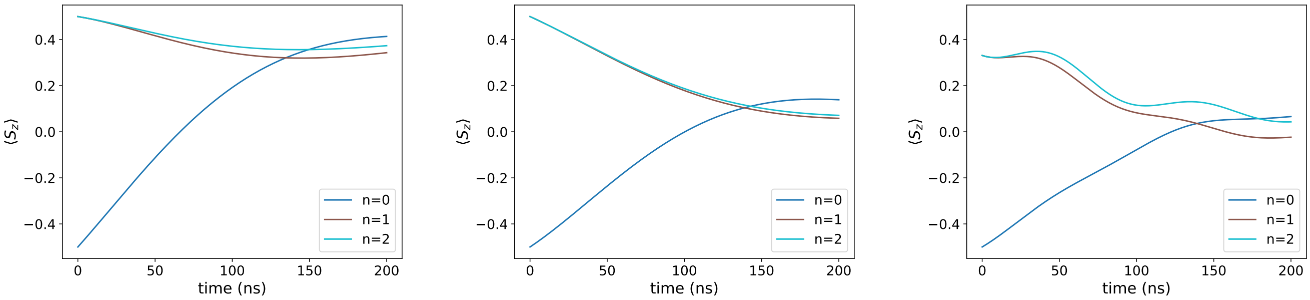

(j) $r = 8{:}\ 2.5 \cdot 10^{1}$ GHz (k) $r = 8{:}\ 2.5 \cdot 10^{-1}$ GHz (l) $r = 8{:}\ 2.5 \cdot 10^{-3}$ GHz

Figure 5.13: Time evolution of the expectation value of the $S_z$ component for a triangle structure of three spins configured at interatomic distances $r = 4, 6, 8$ lattice constants. The rows represent distances $r = 4, 6, 8$, where the second rows provides a zoomed in frame at 0 to 10 nanoseconds of the first row, while the columns correspond to different applied magnetic fields decreasing from left to right.

### 5.3.3 Hexagonal Lattice

Next, we consider the hexagonal structure for distances $r = 4, 5, 6$ lattice constants, ranging from a dominant exchange coupling to a dominant dipolar coupling, as discussed in Section 5.1. The applied magnetic field is varied from $2.5 \cdot 10^1$ GHz to $2.5 \cdot 10^{-3}$ GHz along the $z$-axis, perpendicular to the system. The system is initialised in its equilibrium state, which depends on both the interatomic distance and magnetic field strength. For a strong magnetic field, the equilibrium state is $|\uparrow\rangle_7 = |\uparrow\uparrow\uparrow\uparrow\uparrow\uparrow\uparrow\rangle$, whereas for zero magnetic field, the equilibrium state corresponds to the doublet state of a seven-spin system. When considering a hexagon without its central spin, the equilibrium state is $|\uparrow\rangle_6$ for a strong magnetic field and the singlet state for a weak magnetic field. For any intermediate magnetic field, the system either resembles the doublet or singlet state but increasingly favours $|\uparrow\rangle_7$ or $|\uparrow\rangle_6$ in proportion to the magnetic field strength.
For the hexagonal structure, there are multiple configurations:

(a) A hexagon without a central spin, where one outer spin is flipped.

(b) A hexagon with a central spin, where an outer spin is flipped.

(c) A hexagon with a central spin, where the central spin itself is flipped.

The results of the first case (without a central spin) are variations of the second two cases (including a central spin). Thus, we leave the six-spin hexagon without a central spin for Appendix B.1. For the two seven-spin hexagonal structures, Figures 5.15 and 5.16 show the time evolution of the spins of a hexagon with a central spin when an outer spin ($n = 0$) or the middle spin ($n = 6$) is flipped, respectively. The numbering of the spins is visualised in Figure 5.14.

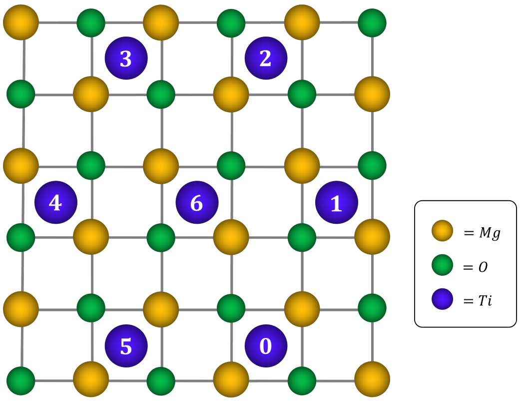

Figure 5.14: Hexagonal spin structure on a square MgO lattice, including spin numbering. (Copy of Figure 5.9)

#### Outer Spin Flip

Figure 5.15 shows the time evolution of a hexagon with a central spin, where spin $n = 0$ is flipped for the distances and magnetic field strengths discussed in the previous section. The specific choice of which outer spin to flip is nearly inconsequential due to the symmetry of the hexagon, apart from minor deviations introduced by the square lattice on which the hexagon is placed.
At a distance of $r = 4$ lattice constants, the exchange coupling is approximately $10^3$ GHz (Figure 5.15), making the previously used time step of $\Delta t = 0.2$ ns insufficiently small, resulting in aliasing in Figures 5.15a, 5.15b, 5.15c. To address this, the second row of Figure 5.15 presents zoomed-in frames over a 10 ns window, using a refined time step of $\Delta t = 5 \cdot 10^{-3}$ ns.

At $r = 4$, the exchange coupling dominates, leading to high-frequency oscillations. Only from a distance of $r = 5$ lattice constants do the results exhibit a recognizable pattern, similar to the square lattice, where pairs of spins primarily interact with each other. Like for the triangle, in Section 5.3.2, the neighbouring spins (0) (flipped) and (5) form the base of a symmetric partition of the hexagon. As a result, the decoherence pattern shows similarities with respect to the triangular structure. For a strong magnetic field at $r = 5$ in Figure 5.15g, spins (0) and (5) oscillate asymmetrically, while they exert minimal influence on spins (1) and (4), which oppose each other and exhibit only small oscillations. The oscillations of spins (0) and (5) also show periodic behaviour, closely followed by the asymmetric oscillations of spins (2) and (3), which are positioned opposite to (0) and (5). The middle spin exhibits independent oscillations, out of phase with respect to the other spins.

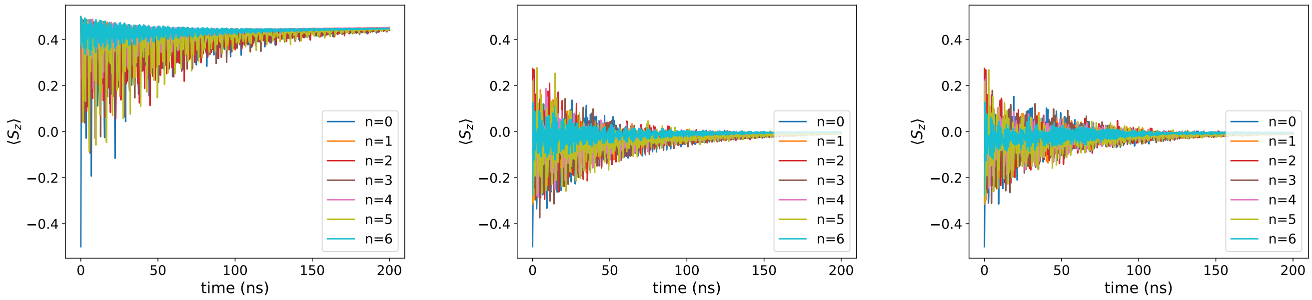

(a) $r = 4$: $2.5 \cdot 10^{1}$ GHz

(b) $r = 4$: $2.5 \cdot 10^{-1}$ GHz

(c) $r = 4$: $2.5 \cdot 10^{-3}$ GHz

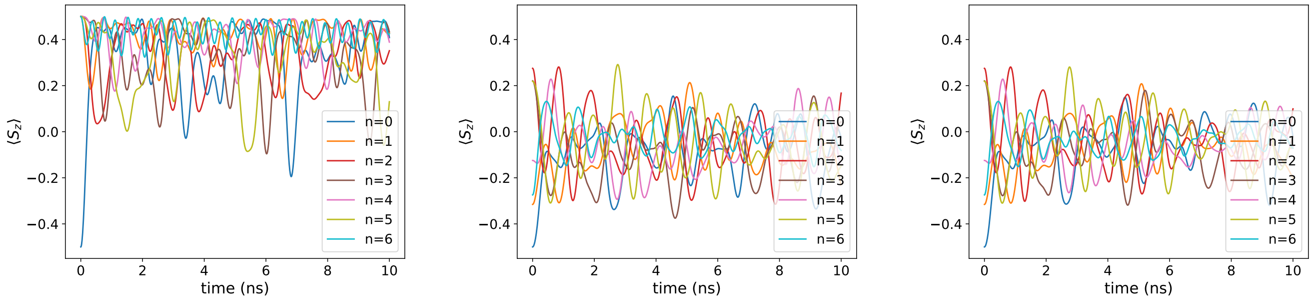

(d) 0-10 ns frame figure (a)

(e) 0-10 ns frame figure (b)

(f) 0-10 ns frame figure (c)

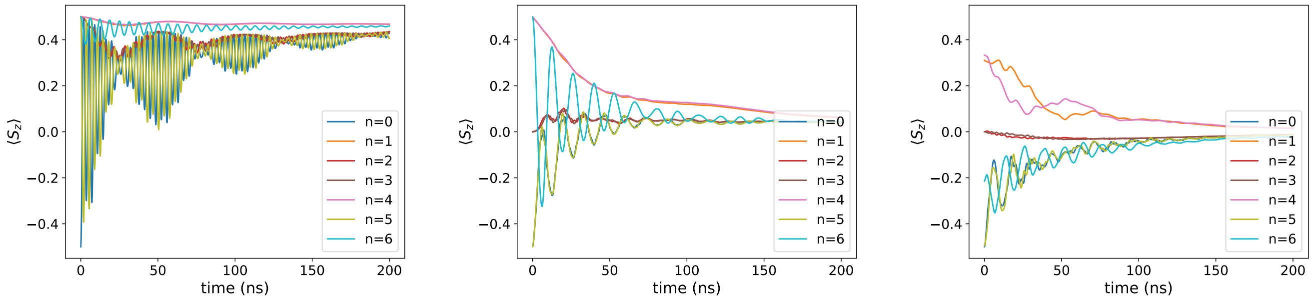

(g) $r = 5$: $2.5 \cdot 10^{1}$ GHz

(h) $r = 5$: $2.5 \cdot 10^{-1}$ GHz

(i) $r = 5$: $2.5 \cdot 10^{-3}$ GHz

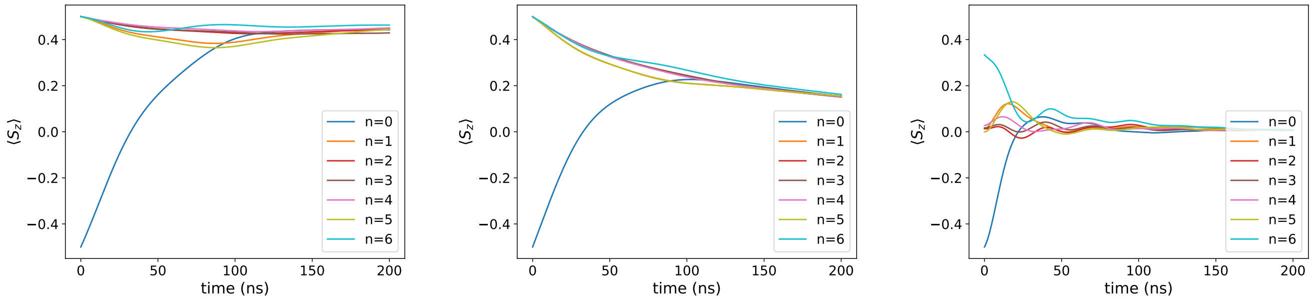

(j) $r = 6$: $2.5 \cdot 10^{1}$ GHz

(k) $r = 6$: $2.5 \cdot 10^{-1}$ GHz

(l) $r = 6$: $2.5 \cdot 10^{-3}$ GHz

Figure 5.15: Time evolution of the expectation value of the $S_z$ component over 0 to 200 nanoseconds for a hexagonal 7-spin configuration, where an outer circle spin is flipped at $t = 0$. The rows represent distances $r = 4, 5, 6$, where the second rows provides a zoomed in frame at 0 to 10 nanoseconds of the first row, while the columns correspond to different applied magnetic fields decreasing from left to right.

In case of a weaker magnetic field shown in Figure 5.15h, the oscillation amplitudes of all spins decrease, except for the middle spin, which shows an absolute increase in oscillation amplitude. The middle spin (6), which forms a triangle with spins (0) and (5), now oscillates asymmetrically with respect to spins (0) and (5), which themselves oscillate more slowly and symmetrically. The other spin pairs, (1) and (4), and (2) and (3), continue to exhibit similar behaviour as before. This trend persists for an even weaker magnetic as shown field in Figure 5.15i.

At larger interatomic distances, the nature of spin pair interactions changes. Whereas previously the flipped spin (0) primarily interacted with its closest neighbour (5), it now interacts approximately equally with both spins (5) and (1). Spin (6), equidistant from (1) and (5), continues to oscillate independently, while the opposite spins (2), (3), (4) form a trio, which gradually splits up as the magnetic field strength decreases as in Figure 5.15l.

### Middle Spin Flip

Figure 5.16 shows the time evolution of a hexagon with a central spin, where the middle spin (6) is flipped for the same distances and magnetic field strengths discussed in the previous section. As described for the square lattice and the previous hexagonal structure, the second row of Figure 5.16 presents zoomed-in frames over a window of 10 ns, using a refined time step of $\Delta t = 5 \cdot 10^{-3}$ ns.

In contrast to the spin (0) flip, the results for decoherence due to the middle spin (6) flip in the exchange-dominated region at $r = 4$ show significantly more coherent behaviour. Figure 5.16d reveals three distinct oscillation patterns: blue oscillations for the flipped spin (6), pink oscillations for spins (1) and (4), and green oscillations for spins (0), (2), (3), and (5). Due to the asymmetry in the hexagon, the latter four spins are closer to the middle spin compared to spins (1) and (4). As a result, their oscillations are out of phase and the closer spins exhibit slightly larger amplitudes.

The middle spin oscillates asymmetrically with respect to the outer spins, displaying large peaks corresponding to the oscillations of the closer spins and smaller peaks for the more distant spins. Additionally, the oscillations of the middle spin (6) exhibit periodic behaviour. The case of a strong magnetic field in Figure 5.16d separates the oscillation patterns, while for weaker magnetic fields in Figures 5.16e, 5.16f, these oscillations increasingly overlap along the $\langle S_z \rangle$-axis.

For larger interatomic distances, the oscillation frequencies decrease, as seen in Figure 5.16g. Here, the effect of the increased distance between spins (1) and (4) and the middle spin (6) becomes apparent. When the magnetic field strength is reduced at $r = 5$, the equilibrium value initially decreases in the graph of Figure 5.16h. However, at the near-zero magnetic field of Figure 5.16i, the oscillations of spin pairs (0) and (3), and (2) and (5), which were previously in phase, become asymmetric. Interestingly, at this magnetic field strength, for both smaller and larger interatomic distances, these oscillations return to an in-phase behaviour with slight deviations, as seen in Figure 5.16f. Moreover, at $r = 5$, for a strong magnetic field, the middle spin primarily interacts with its nearest neighbouring spins (0), (2), (3), and (5). However, for a weak magnetic field, the dominant interaction shifts to the middle spin and its more distant neighbours (1) and (4). This trend is also observed for $r = 4$.

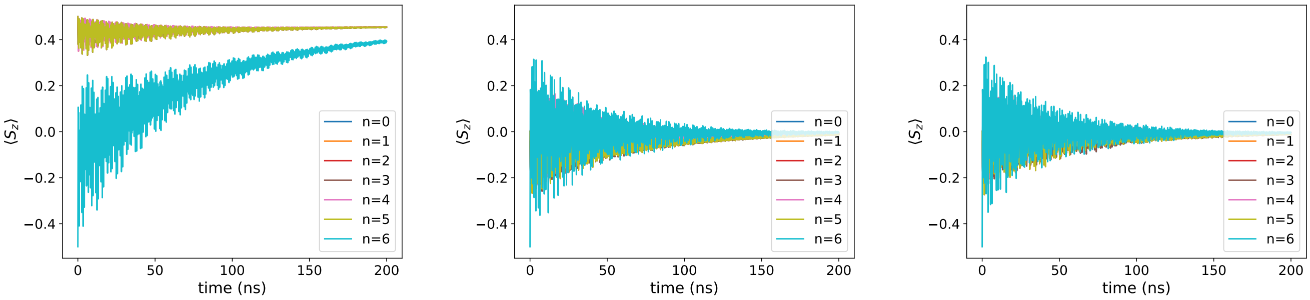

(a) $r = 4{:}\ 2.5 \cdot 10^1$ GHz (b) $r = 4{:}\ 2.5 \cdot 10^{-1}$ GHz (c) $r = 4{:}\ 2.5 \cdot 10^{-3}$ GHz

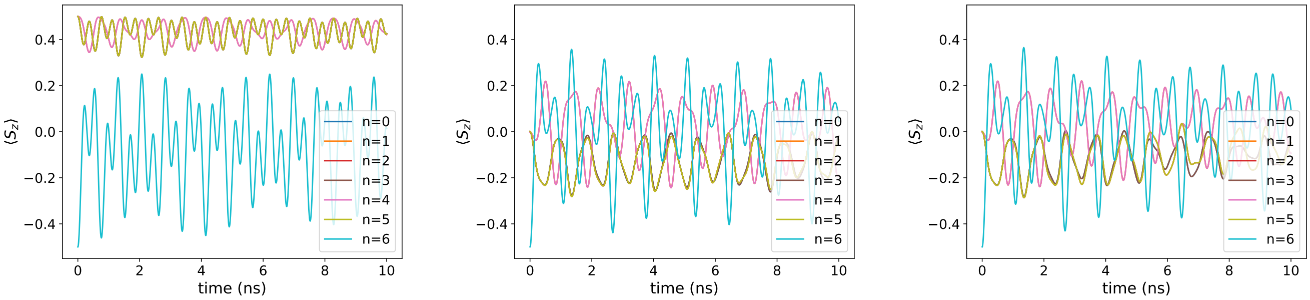

(d) 0-10 ns frame figure (a) (e) 0-10 ns frame figure (a) (f) 0-10 ns frame figure (a)

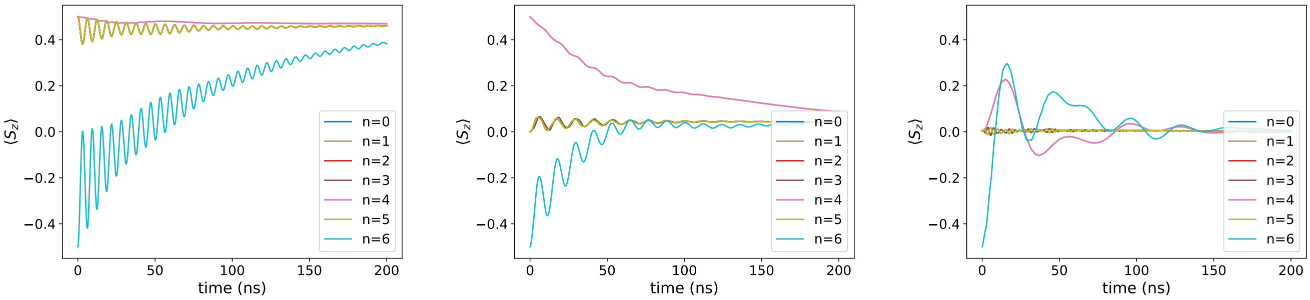

(g) $r = 5{:}\ 2.5 \cdot 10^1$ GHz (h) $r = 5{:}\ 2.5 \cdot 10^{-1}$ GHz (i) $r = 5{:}\ 2.5 \cdot 10^{-3}$ GHz

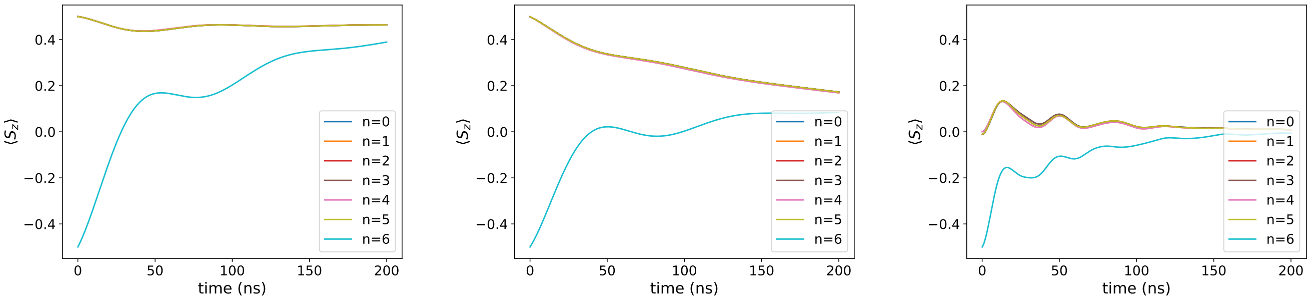

(j) $r = 6{:}\ 2.5 \cdot 10^1$ GHz (k) $r = 6{:}\ 2.5 \cdot 10^{-1}$ GHz (l) $r = 6{:}\ 2.5 \cdot 10^{-3}$ GHz

Figure 5.16: Time evolution of the expectation value of the $S_z$ component over 0 to 200 nanoseconds for a hexagonal 7-spin configuration, where the middle spin is flipped at $t = 0$. The rows represent distances $r = 4, 5, 6$, where the second row provides a zoomed in frame at 0 to 10 nanoseconds of the first row, while the columns correspond to different applied magnetic fields decreasing from left to right.

# Chapter 6

# Conclusions and discussion

This thesis has explored the quantum states and dynamics of two-dimensional spin structures on an MgO lattice, specifically investigating eigenenergies, eigenstates, and decoherence mechanisms in square and hexagonal Ti spin-$\frac{1}{2}$ configurations. Using a combination of analytical calculations and numerical simulations, we examined how interatomic distance and magnetic field strength influence these systems, as well as the role of spin flips in inducing decoherence.

## 6.1 Eigenenergies and Eigenstates

The eigenenergy distributions for the square lattice showed distinct clustering patterns depending on the interatomic distance and applied magnetic field strength. At small distances, exchange coupling dominates, leading to clustered energy levels, whereas at larger distances, dipolar coupling becomes more relevant, resulting in a more evenly spread eigenenergy distribution. As the magnetic field increases, eigenstates reorganise into a binomial pattern, representing distinct spin projection states.

An important observation is the behaviour of the singlet and doublet eigenstates. At low magnetic fields, degeneracies persist between these states due to the inherent symmetries of the system. However, as the magnetic field increases, previously degenerate eigenstates split in energy, following a predictable pattern dictated by their spin projections. Notably, the real-valued superposition of $(\alpha \left|\downarrow\downarrow\uparrow\uparrow\right\rangle + \beta \left|\uparrow\uparrow\downarrow\downarrow\right\rangle)$ and the complex-valued $(\gamma \left|\downarrow\uparrow\downarrow\uparrow\right\rangle + \delta \left|\uparrow\downarrow\uparrow\downarrow\right\rangle)$ remain degenerate even under increasing field strength, distinguishing them from other eigenstate pairs that separate proportionally with the applied field. This trend persists across both the square and hexagonal lattices, although additional symmetry constraints in the hexagonal configuration could modify the precise splitting behaviour.

For the hexagonal lattice, a similar trend was expected. However, additional geometric constraints introduce further degeneracies and modified coupling effects. Expanding the triangle lattice results to the hexagonal configuration would require considering the varying placement sites within the MgO lattice, which affect the effective coupling strengths. The transition from the exchange to the dipolar coupling regimes follows similar patterns, though the increased connectivity in the hexagonal geometry could alter the precise eigenenergy spacing and state mixing.

## 6.2 Spin Flip Decoherence

Decoherence was analysed by inducing a spin flip and observing the subsequent evolution of the system. In the square lattice, flipping any spin preserves symmetry, leading to more uniform decoherence patterns. The hexagonal lattice also exhibited symmetry both in the case of a middle or outer spin flip, where the perturbation distributed across the structure depending on the precise interatomic distance, maintaining a predictable decay profile.

However, depending on the spacing difference in the hexagonal lattice, the system evolves differently due to the exchange or dipolar coupling being dominant. This effect arises due to destructive interference when interactions are out of phase because of asymmetries in the hexagon on the square lattice, opposed to a perfect hexagon of equidistant spins. The resulting decoherence dynamics differ significantly from the centrally induced flip, highlighting the importance of geometric arrangement in determining spin stability.

## 6.3 Broader Implications and Future Work

The findings of this study have implications for understanding spin coherence in engineered quantum systems. The transition between exchange and dipolar coupling regimes provides insight into the tunability of spin interactions, which is relevant for quantum simulation and information processing applications. Additionally, spin-flip-induced decoherence patterns suggest that structural symmetries can be leveraged to improve spin coherence times, potentially aiding in the design of more robust quantum systems.

Future research could focus on extending these models to larger lattice structures, incorporating more complex geometries beyond simple square and hexagonal patterns. Additionally, exploring the effects of different placement sites on the MgO lattice, as well as including external perturbations such as local strain or anisotropic interactions, could provide a more comprehensive understanding of spin decoherence mechanisms.

Overall, the results demonstrate the interplay between the geometry of the atomic configuration, coupling strengths, and decoherence in two-dimensional spin structures, laying the groundwork for further investigations into controlled spin dynamics in quantum materials.

# Appendices

# Appendix A

# Nearest-Neighbour Approximation

## A.1 Square Lattice

For the square lattice we consider the structure shown in figure A.1 with $N_x = N_y = 2$. The atoms are numbered along the $x$- and $y$-axis with $(i, j)$, which is necessary to define the Hamiltonian. In the following enumeration, we consider the different interactions independently for a square lattice structure of $N_x \times N_y$ atoms.

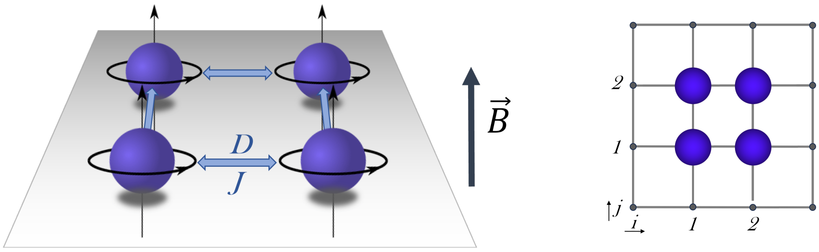

(a) Frontal view (b) Top view

Figure A.1: Example of a two-dimensional square lattice of atoms aligned in a ferromagnetic configuration with an applied magnetic field **B**. (a) Frontal view, where neighbouring atoms experience both Heisenberg exchange coupling $J$ and dipole-dipole coupling $r$, which are represented by interactions between adjacent atoms in the lattice. (b) Top view, denoting lattice axes and atom numbering.

### Zeeman Interaction

$$\hat{H}_{\mathrm{Z}} = \mu_B g \sum_{i=1}^{N_x} \sum_{j=1}^{N_y} \mathbf{B} \cdot \hat{\mathbf{S}}^{(i,j)}. \tag{A.1}$$

### Heisenberg Exchange Coupling

For simplicity we split this up in two directions: the exchange coupling in the $x$-direction, and in the $y$-direction and sum the Hamiltonian over $N_x \times N_y$ atoms, resulting in the general square lattice Hamiltonian:

$$\hat{H}_{\mathrm{Exc}} = J \sum_{i=1}^{N_x-1} \sum_{j=1}^{N_y} \hat{\mathbf{S}}^{(i,j)} \cdot \hat{\mathbf{S}}^{(i+1,j)} + J \sum_{i=1}^{N_x} \sum_{j=1}^{N_y-1} \hat{\mathbf{S}}^{(i,j)} \cdot \hat{\mathbf{S}}^{(i,j+1)}. \tag{A.2}$$

### Dipole-Dipole Coupling

We apply equation (3.13) from Section 3.1.3 with $n_x$ the unit vector between atom $(i, j)$ and $(i + 1, j)$ and $n_y$ the unit vector between atom $(i, j)$ and $(i, j + 1)$, to obtain:

$$
\begin{aligned}
\hat{H}_{\mathrm{D}} =& D_0 \sum_{i=1}^{N_x-1} \sum_{j=1}^{N_y} \left[ -2\hat{S}_x^{(i,j)} \hat{S}_x^{(i+1,j)} + \hat{S}_y^{(i,j)} \hat{S}_y^{(i+1,j)} + \hat{S}_z^{(i,j)} \hat{S}_z^{(i+1,j)} \right] + \\
& D_0 \sum_{i=1}^{N_x} \sum_{j=1}^{N_y-1} \left[ \hat{S}_x^{(i,j)} \hat{S}_x^{(i+1,j)} - 2\hat{S}_y^{(i,j)} \hat{S}_y^{(i+1,j)} + \hat{S}_z^{(i,j)} \hat{S}_z^{(i+1,j)} \right].
\end{aligned} \tag{A.3}
$$

### Nearest Neighbour Square Lattice Hamiltonian

The sum of the Zeeman, exchange and dipole Hamiltonian for the $N_x \times N_y$ lattice is:

$$
\begin{aligned}
\hat{H}_{2\mathrm{D}} =& \mu_B g \sum_{i=1}^{N_x} \sum_{j=1}^{N_y} \mathbf{B} \cdot \hat{\mathbf{S}}^{(i,j)} + \\
& \sum_{i=1}^{N_x-1} \sum_{j=1}^{N_y} \left[ (J - 2D_0)\, \hat{S}_x^{(i,j)} \hat{S}_x^{(i+1,j)} + (J + D_0)\, \hat{S}_y^{(i,j)} \hat{S}_y^{(i+1,j)} + (J + D_0)\, \hat{S}_z^{(i,j)} \hat{S}_z^{(i+1,j)} \right] + \\
& \sum_{i=1}^{N_x} \sum_{j=1}^{N_y-1} \left[ (J + D_0)\, \hat{S}_x^{(i,j)} \hat{S}_x^{(i+1,j)} (J - 2D_0)\, \hat{S}_y^{(i,j)} \hat{S}_y^{(i+1,j)} + (J + D_0)\, \hat{S}_z^{(i,j)} \hat{S}_z^{(i+1,j)} \right].
\end{aligned} \tag{A.4}
$$

## A.2 Triangular Lattice

The triangular lattice, illustrated in Figure 3.2.2, follows the same atomic numbering in the $xy$-plane as the square lattice. We consider a hexagon on a lattice of $N_x \times N_y = 3 \times 3$

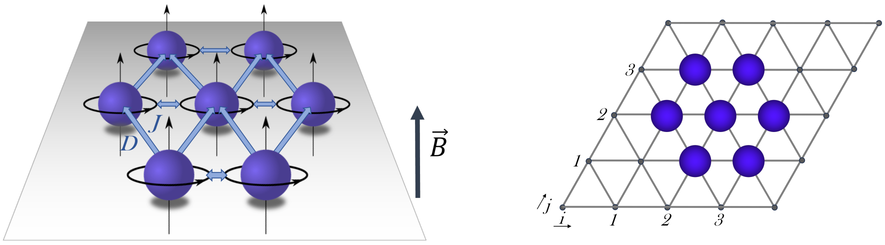

(a) Frontal view

(b) Top view

Figure A.2: $3 \times 3$ hexagon in a two-dimensional triangular lattice of atoms aligned in a ferromagnetic configuration with an applied magnetic field $\mathbf{B}$. a) Frontal view, where neighbouring atoms experience both Heisenberg exchange coupling $J$ and dipole-dipole coupling $r$, which are represented by interactions between adjacent atoms in the lattice. b) Top view, denoting lattice axes and atom numbering.

### Zeeman Interaction

To sum over the atoms in a hexagonal structure, the hexagon is cut in a lower and upper half, depicted in the Zeeman Hamiltonian in equation A.5. We employ this notation for all formulas regarding the triangular lattice.

$$
\hat{H}_{\mathrm{Z}} = \mu_B g \sum_{j=1}^{\frac{N_x-1}{2}} \sum_{i=\frac{N_x+3}{2}-j}^{N_x} \mathbf{B} \cdot \hat{\mathbf{S}}^{(i,j)} + \mu_B g \sum_{j=\frac{N_x+1}{2}}^{N_x} \sum_{i=1}^{\frac{3N_x+1}{2}-j} \mathbf{B} \cdot \hat{\mathbf{S}}^{(i,j)} \tag{A.5}
$$

## Heisenberg Exchange Coupling

For the triangular lattice, we can modify the Hamiltonian used for the square lattice in equation (A.2) to match the boundary conditions of the hexagon. The resulting expression in equation (A.6) in the first line accounts for the horizontal interactions along the $i$-axis, as shown in Figure A.2b, second the interactions along the $j$-axis, and third the interactions along the axis of coordinates $(i, j-1)$.

$$
\begin{aligned}
\hat{H}_{\text{Exc}} = & J \sum_{j=1}^{\frac{N_x-1}{2}} \sum_{i=\frac{N_x+3}{2}-j}^{N_x-1} \hat{\mathbf{S}}^{(i,j)} \cdot \hat{\mathbf{S}}^{(i+1,j)} + J \sum_{j=\frac{N_x+1}{2}}^{N_x} \sum_{i=1}^{\frac{3N_x-1}{2}-j} \hat{\mathbf{S}}^{(i,j)} \cdot \hat{\mathbf{S}}^{(i+1,j)} + \\
& J \sum_{j=1}^{\frac{N_x-1}{2}} \sum_{i=\frac{N_x+3}{2}-j}^{N_x} \hat{\mathbf{S}}^{(i,j)} \cdot \hat{\mathbf{S}}^{(i,j+1)} + J \sum_{j=\frac{N_x+1}{2}}^{N_x-1} \sum_{i=1}^{\frac{3N_x-1}{2}-j} \hat{\mathbf{S}}^{(i,j)} \cdot \hat{\mathbf{S}}^{(i,j+1)} + \\
& J \sum_{j=1}^{\frac{N_x-1}{2}} \sum_{i=\frac{N_x+3}{2}-j}^{N_x} \hat{\mathbf{S}}^{(i,j)} \cdot \hat{\mathbf{S}}^{(i-1,j+1)} + J \sum_{j=\frac{N_x+1}{2}}^{N_x-1} \sum_{i=2}^{\frac{3N_x-1}{2}-j} \hat{\mathbf{S}}^{(i,j)} \cdot \hat{\mathbf{S}}^{(i-1,j+1)}.
\end{aligned}
\tag{A.6}
$$

## Dipole-Dipole Coupling

Similarly, the dipole-dipole interactions for the hexagonal lattice can be defined for three directions.

$$
\begin{aligned}
\hat{H}_{\text{D}} = & \sum_{j=1}^{\frac{N_x-1}{2}} \sum_{i=\frac{N_x+3}{2}-j}^{N_x-1} \left[\hat{\mathbf{S}}^{(i,j)} \cdot \hat{\mathbf{S}}^{(i+1,j)} - 3\left(\hat{\mathbf{S}}^{(i,j)} \cdot n\right)\left(\hat{\mathbf{S}}^{(i+1,j)} \cdot n\right)\right] + \\
& \sum_{j=\frac{N_x+1}{2}}^{N_x} \sum_{i=1}^{\frac{3N_x-1}{2}-j} \left[\hat{\mathbf{S}}^{(i,j)} \cdot \hat{\mathbf{S}}^{(i+1,j)} - 3\left(\hat{\mathbf{S}}^{(i,j)} \cdot n\right)\left(\hat{\mathbf{S}}^{(i+1,j)} \cdot n\right)\right] + \\
& \sum_{j=1}^{\frac{N_x-1}{2}} \sum_{i=\frac{N_x+3}{2}-j}^{N_x} \left[\hat{\mathbf{S}}^{(i,j)} \cdot \hat{\mathbf{S}}^{(i,j+1)} - 3\left(\hat{\mathbf{S}}^{(i,j)} \cdot n\right)\left(\hat{\mathbf{S}}^{(i,j+1)} \cdot n\right)\right] + \\
& \sum_{j=\frac{N_x+1}{2}}^{N_x-1} \sum_{i=1}^{\frac{3N_x-1}{2}-j} \left[\hat{\mathbf{S}}^{(i,j)} \cdot \hat{\mathbf{S}}^{(ij+1)} - 3\left(\hat{\mathbf{S}}^{(i,j)} \cdot n\right)\left(\hat{\mathbf{S}}^{(i,j+1)} \cdot n\right)\right] + \\
& \sum_{j=1}^{\frac{N_x-1}{2}} \sum_{i=\frac{N_x+3}{2}-j}^{N_x} \left[\hat{\mathbf{S}}^{(i,j)} \cdot \hat{\mathbf{S}}^{(i-1,j+1)} - 3\left(\hat{\mathbf{S}}^{(i,j)} \cdot n\right)\left(\hat{\mathbf{S}}^{(i-1,j+1)} \cdot n\right)\right] + \\
& \sum_{j=\frac{N_x+1}{2}}^{N_x-1} \sum_{i=2}^{\frac{3N_x-1}{2}-j} \left[\hat{\mathbf{S}}^{(i,j)} \cdot \hat{\mathbf{S}}^{(i-1,j+1)} - 3\left(\hat{\mathbf{S}}^{(i,j)} \cdot n\right)\left(\hat{\mathbf{S}}^{(i-1,j+1)} \cdot n\right)\right]
\end{aligned}
\tag{A.7}
$$

## Nearest Neighbour Square Lattice Hamiltonian

The complete Hamiltonian for a triangular lattice of $N_x \times N_y$ with both exchange and dipole-dipole couplings for interactions at angles $\theta_1 = \arctan \frac{2}{1}$ and $\theta_2 = \arctan \frac{2}{-1}$ is:

$$
\begin{aligned}
\hat{H}_{2\mathrm{D}} =& \mu_B g \sum_{j=1}^{\frac{N_x-1}{2}} \sum_{i=\frac{N_x+3}{2}-j}^{N_x} \mathbf{B} \cdot \hat{\mathbf{S}}^{(i,j)} + \mu_B g \sum_{j=\frac{N_x+1}{2}}^{N_x} \sum_{i=1}^{\frac{3N_x+1}{2}-j} \mathbf{B} \cdot \hat{\mathbf{S}}^{(i,j)} + \\
& \sum_{j=1}^{\frac{N_x-1}{2}} \sum_{i=\frac{N_x+3}{2}-j}^{N_x-1} \Big[ (J - 2D_0)\, \hat{S}_x^{(i,j)} \hat{S}_x^{(i+1,j)} + (J + D_0)\, \hat{S}_y^{(i,j)} \hat{S}_y^{(i+1,j)} + (J + D_0)\, \hat{S}_z^{(i,j)} \hat{S}_z^{(i+1,j)} \Big] + \\
& \sum_{j=\frac{N_x+1}{2}}^{N_x} \sum_{i=1}^{\frac{3N_x-1}{2}-j} \Big[ (J - 2D_0)\, \hat{S}_x^{(i,j)} \hat{S}_x^{(i+1,j)} + (J + D_0)\, \hat{S}_y^{(i,j)} \hat{S}_y^{(i+1,j)} + (J + D_0)\, \hat{S}_z^{(i,j)} \hat{S}_z^{(i+1,j)} \Big] + \\
& \sum_{j=1}^{\frac{N_x-1}{2}} \sum_{i=\frac{N_x+3}{2}-j}^{N_x} \Bigg[ \left( J + \frac{2D_0}{5} \right) \hat{S}_x^{(i,j)} \hat{S}_x^{(i+1,j)} + \left( J - \frac{7D_0}{5} \right) \hat{S}_y^{(i,j)} \hat{S}_y^{(i+1,j)} + (J + D_0)\, \hat{S}_z^{(i,j)} \hat{S}_z^{(i+1,j)} \\
& \qquad\qquad - \frac{12D_0}{5} \left( \hat{S}_x^{(i,j)} \hat{S}_y^{(i,j+1)} + \hat{S}_x^{(i,j+1)} \hat{S}_y^{(i,j)} \right) \Bigg] + \\
& \sum_{j=\frac{N_x+1}{2}}^{N_x-1} \sum_{i=1}^{\frac{3N_x-1}{2}-j} \Bigg[ \left( J + \frac{2D_0}{5} \right) \hat{S}_x^{(i,j)} \hat{S}_x^{(i+1,j)} + \left( J - \frac{7D_0}{5} \right) \hat{S}_y^{(i,j)} \hat{S}_y^{(i+1,j)} + (J + D_0)\, \hat{S}_z^{(i,j)} \hat{S}_z^{(i+1,j)} \\
& \qquad\qquad - \frac{12D_0}{5} \left( \hat{S}_x^{(i,j)} \hat{S}_y^{(i,j+1)} + \hat{S}_x^{(i,j+1)} \hat{S}_y^{(i,j)} \right) \Bigg] + \\
& \sum_{j=1}^{\frac{N_x-1}{2}} \sum_{i=\frac{N_x+3}{2}-j}^{N_x} \Bigg[ \left( J + \frac{2D_0}{5} \right) \hat{S}_x^{(i,j)} \hat{S}_x^{(i+1,j)} + \left( J - \frac{7D_0}{5} \right) \hat{S}_y^{(i,j)} \hat{S}_y^{(i+1,j)} + (J + D_0)\, \hat{S}_z^{(i,j)} \hat{S}_z^{(i+1,j)} \\
& \qquad\qquad + \frac{12D_0}{5} \left( \hat{S}_x^{(i,j)} \hat{S}_y^{(i,j+1)} + \hat{S}_x^{(i,j+1)} \hat{S}_y^{(i,j)} \right) \Bigg] + \\
& \sum_{j=\frac{N_x+1}{2}}^{N_x-1} \sum_{i=2}^{\frac{3N_x-1}{2}-j} \Bigg[ \left( J + \frac{2D_0}{5} \right) \hat{S}_x^{(i,j)} \hat{S}_x^{(i+1,j)} + \left( J - \frac{7D_0}{5} \right) \hat{S}_y^{(i,j)} \hat{S}_y^{(i+1,j)} + (J + D_0)\, \hat{S}_z^{(i,j)} \hat{S}_z^{(i+1,j)} \\
& \qquad\qquad + \frac{12D_0}{5} \left( \hat{S}_x^{(i,j)} \hat{S}_y^{(i,j+1)} + \hat{S}_x^{(i,j+1)} \hat{S}_y^{(i,j)} \right) \Bigg]
\end{aligned}
\tag{A.8}
$$

# Appendix B

# Decoherence in Spin Systems

## B.1 Hexagonal Lattice

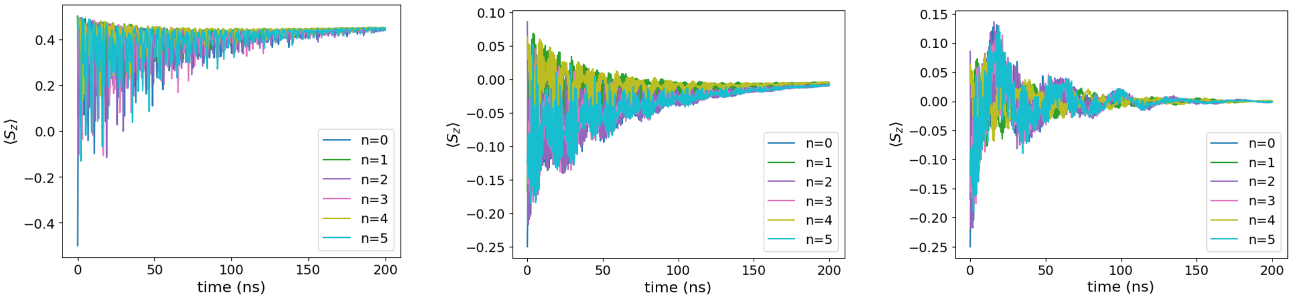

(a) $r = 4$: $2.5 \cdot 10^1$ GHz

(b) $r = 4$: $2.5 \cdot 10^{-1}$ GHz

(c) $r = 4$: $2.5 \cdot 10^{-3}$ GHz

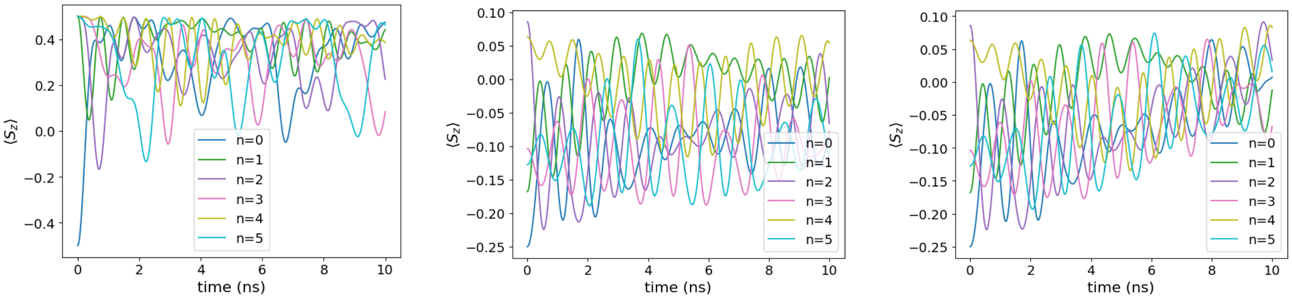

(d) 0-10 ns frame figure (a)

(e) 0-10 ns frame figure (b)

(f) 0-10 ns frame figure (b)

Figure B.1: Time evolution of the expectation value of the $S_z$ component over 0 to 200 nanoseconds for a hexagonal 6-spin configuration, where an outer circle spin is flipped at $t = 0$. The rows represent distances $r = 4$, where the second row provides a zoomed in frame at 0 to 10 nanoseconds of the first row, while the columns correspond to different external magnetic fields decreasing from left to right.

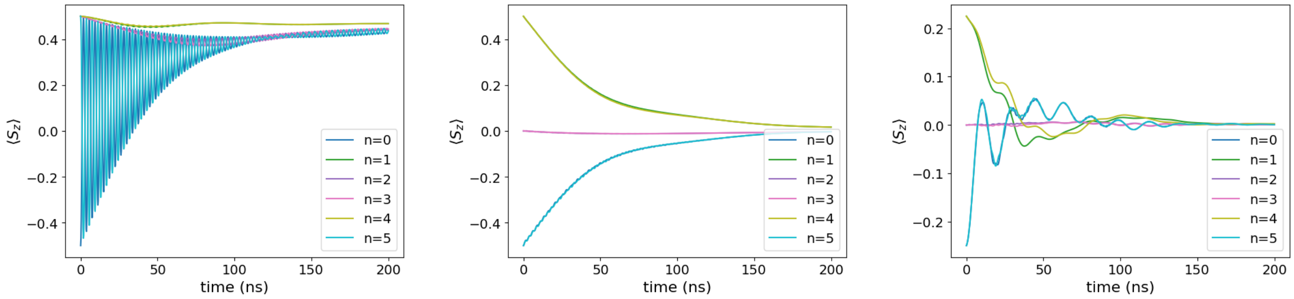

(a) $r = 5$: $2.5 \cdot 10^{1}$ GHz (b) $r = 5$: $2.5 \cdot 10^{-1}$ GHz (c) $r = 5$: $2.5 \cdot 10^{-3}$ GHz

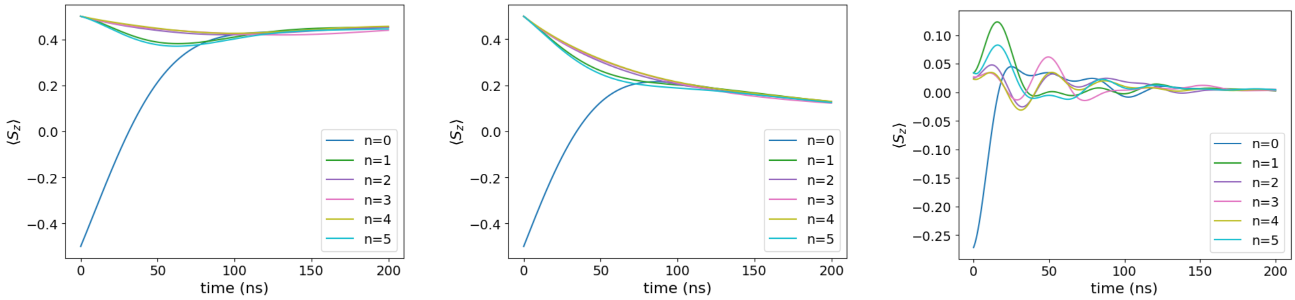

(d) $r = 6$: $2.5 \cdot 10^{1}$ GHz (e) $r = 6$: $2.5 \cdot 10^{-1}$ GHz (f) $r = 6$: $2.5 \cdot 10^{-3}$ GHz

Figure B.2: Continuation of Figure B.1. Time evolution of the expectation value of the $S_z$ component over 0 to 200 nanoseconds for a hexagonal 6-spin configuration, where an outer circle spin is flipped at $t = 0$. The rows represent distances $r = 5, 6$, while the columns correspond to different external magnetic fields decreasing from left to right.

# Bibliography

[1] CERN. *The Standard Model.* Accessed: 2025-03-17. 2024. URL: `https://home.cern/science/physics/standard-model`.

[2] Sander Otte. *OtteLab.* `https://ottelab.tudelft.nl/research/`. [Online; last accessed 01-October-2024]. 2024.

[3] Gerd Binnig and Heinrich Rohrer. “Scanning tunneling microscopy—from birth to adolescence”. In: *reviews of modern physics* 59.3 (1987), p. 615.

[4] Donald M Eigler and Erhard K Schweizer. “Positioning single atoms with a scanning tunnelling microscope”. In: *Nature* 344.6266 (1990), pp. 524–526.

[5] A. Spinelli. “Quantum Magnetism through Atomic Assembly”. PhD thesis. Delft University of Technology, 2015.

[6] Lukas M. Veldman et al. “Free coherent evolution of a coupled atomic spin system initialized by electron scattering”. In: *Science* 372.6545 (2021), pp. 964–968. DOI: `10.1126/science.abg8223`. eprint: `https://www.science.org/doi/pdf/10.1126/science.abg8223`. URL: `https://www.science.org/doi/abs/10.1126/science.abg8223`.

[7] F Delgado and Joaquín Fernández-Rossier. “Spin decoherence of magnetic atoms on surfaces”. In: *Progress in Surface Science* 92.1 (2017), pp. 40–82.

[8] Daniel Manzano. “A short introduction to the Lindblad master equation”. In: *AIP Advances* 10.2 (Feb. 2020), p. 025106. ISSN: 2158-3226. DOI: `10.1063/1.5115323`. eprint: `https://pubs.aip.org/aip/adv/article-pdf/doi/10.1063/1.5115323/12881278/025106\_1\_online.pdf`. URL: `https://doi.org/10.1063/1.5115323`.

[9] Ernst Ruska. “The development of the electron microscope and of electron microscopy”. In: *Bioscience Reports* 7 (8 1987). ISSN: 15734935. DOI: `10.1007/BF01127674`.

[10] Kai Yang et al. “Engineering the eigenstates of coupled spin-1/2 atoms on a surface”. In: *Physical Review Letters* 119.22 (2017), p. 227206.

[11] LM Veldman. “Coherent dynamics of atomic spins on a surface”. In: *Delft Repositories* (2024).

[12] Ludwig Bartels, Gerhard Meyer, and K-H Rieder. “Basic steps of lateral manipulation of single atoms and diatomic clusters with a scanning tunneling microscope tip”. In: *Physical Review Letters* 79.4 (1997), p. 697.

[13] Chandana Ghosh, Abdelkader Kara, and Talat S Rahman. “Theoretical aspects of vertical and lateral manipulation of atoms”. In: *Surface science* 502 (2002), pp. 519–526.

[14] Barry C Stipe, Mohammad A Rezaei, and Wilson Ho. “Single-molecule vibrational spectroscopy and microscopy”. In: *Science* 280.5370 (1998), pp. 1732–1735.

[15] Roland Wiesendanger. “Spin mapping at the nanoscale and atomic scale”. In: *Reviews of Modern Physics* 81.4 (2009), pp. 1495–1550.

[16] Sebastian Loth et al. “Measurement of fast electron spin relaxation times with atomic resolution”. In: *Science* 329.5999 (2010), pp. 1628–1630.

[17] Marit Piek. “The decoherence of spin chains coupled to an electron bath”. In: (2023).

[18] David J Griffiths and Darrell F Schroeter. *Introduction to quantum mechanics.* Cambridge university press, 2018.

[19] Charles P Slichter. *Principles of magnetic resonance.* Vol. 1. Springer Science & Business Media, 2013.

[20] Roderich Moessner and Arthur P Ramirez. “Geometrical frustration”. In: *Physics Today* 59.2 (2006), pp. 24–29.

[21] Sebastian Loth et al. "Controlling the state of quantum spins with electric currents". In: *Nature Physics* 6 (Mar. 2010), pp. 340–344. DOI: `10.1038/nphys1616`.

[22] A. C Hewson and J. Kondo. "Kondo effect". In: *Scholarpedia* 4.3 (2009). revision #91408, p. 7529. DOI: `10.4249/scholarpedia.7529`.

[23] R. Broekhoven. "Models for probing the coherent free flipflop evolution of atomic e ective spin 1/2 dimers with a tunneling microscope". MA thesis. Delft University of Technology, 2020.

[24] Heinz-Peter Breuer and Francesco Petruccione. *The theory of open quantum systems.* Oxford University Press, USA, 2002.

[25] Robert Alicki and Karl Lendi. *Quantum dynamical semigroups and applications.* Vol. 717. Springer Science & Business Media, 2007.

[26] Max Born. "Quantenmechanik der stoßvorgänge". In: *Zeitschrift für physik* 38.11 (1926), pp. 803–827.

[27] Claude Cohen-Tannoudji, Jacques Dupont-Roc, and Gilbert Grynberg. *Atom-photon interactions: basic processes and applications.* John Wiley & Sons, 1998.

[28] Hal Tasaki. *Physics and mathematics of quantum many-body systems.* Vol. 66. Springer, 2020.